ANL/ESD-15/23

Numerical Modeling of the Lake Mary Road Bridge for Foundation Reuse Assessment

April 2015

ANL/ESD-15/23

Numerical Modeling of the Lake Mary Road Bridge for Foundation Reuse Assessment

by
M.A. Sitek, C. Bojanowski, S.A. Lottes
Transportation Research and Analysis Computing Center (TRACC)
Energy Systems Division, Argonne National Laboratory

April 2015

Table of Contents

List of Figures

List of Tables

1. Introduction and Objectives

1.1. Introduction

A widened superstructure for the Lake Mary Road Bridge located southeast of Flagstaff, Arizona is planned. The bridge provides recreational, commuter and local commercial traffic between I-17 to the north and State Route 87 to the south. It also gives access to Lake Mary, Mormon Lake, and Coconino National Forest.

This project uses numerical techniques to assess the structural integrity and capacity of the bridge foundations and, as a result, reduces the risk associated with reusing the same foundation for a new superstructure. Nondestructive test methods of different types were used in combination with the numerical modeling and analysis. The onsite tests included visual inspection, tomography, ground penetrating radar, drilling boreholes and coreholes, and the laboratory tests on recovered samples. The results were utilized to identify the current geometry of the structure with foundation, including the hidden geometry of the abutments and piers, and soil and foundation material properties. This data was used to build the numerical models and run computational analyses on a high performance computer cluster to assess the structural integrity of the bridge and foundations including the suitability of the foundation for reuse with a new superstructure and traffic that will increase the load on the foundations. Computational analysis is more cost-effective and gives an advantage of getting more detailed knowledge about the structural response. It also enables to go beyond non-destructive testing and find the failure conditions without destroying the structure under consideration.

While the computations for a typical case required far more compute resources than what is available on a typical engineering workstation, they were mid-sized jobs on the Argonne TRACC computer clusters. A typical case was run on either 32 or 64 cores, requiring 2 or 4 compute node machines. The compute nodes are interconnected with 40 Gb/s InfiniBand switches, 40 times the data exchange rate of workstations interconnected with Gb/s Ethernet. The low latency high speed interconnect allows the compute nodes to work together on a problem as though they are a single much larger computer. A typical case run on 64 cores was completed in 12 hours. Cases would usually complete overnight allowing review of results the next day.

1.2. Objectives

The part of the research covered by the current report concentrates on using one of these tools - finite element simulation, which could provide broad information on static and dynamic tests before they are performed. The computational model is built to assess what tests can be performed on-site, what quantities can be measured, where they should be measured and what values can be expected. Extensive numerical modeling was done to determine the response of the superstructure, foundations and bedrock to existing loads. The maximum value of equivalent stress in the foundations was established and compared to the load capacity of the structure and load resistance of the bedrock.

The structure chosen for testing is a bridge carrying Lake Mary Road over Willow Valley Creek, 40 miles south of Flagstaff, AZ. Views of the Lake Mary Bridge are presented on Figure 1.1. It is anticipated that it will be rehabilitated, the foundations will be thoroughly evaluated for reuse and the superstructure will be replaced with a wider one supported on the existing substructure.

A computational model of the existing bridge was developed. The model includes both: the superstructure and the foundations, some effort was also made to include the surrounding ground conditions in the model. This holistic approach is not seen very often, usually only one of the parts of the structure is taken into account and the other is represented as an appropriate boundary condition. The numerical simulations cover the following types of load conditions: static analyses - increased dead load, design live loads and dynamic analyses - dynamic vehicular loading, impulse loading.

The level of details in the model assures the confidence in the results, but also requires substantial computing power. A high-performance computer user facility, known as Transportation Analysis and Computing Center (TRACC) provides the necessary resources, such as massively parallel and parallel computing. The computations were performed on two High Performance Compute Clusters, most analysis required two to four 16-core compute nodes.

Figure 1.1: Views of the Lake Mary Bridge

1.3. Site Conditions

Lake Mary Road is primarily used by local residents and commuters as well as regional commercial traffic. The posted speed limit is 55 mph. The bridge is 104-foot long and 34-foot wide with three spans. The bearing-to-bearing distances for the exterior spans is 25 feet and for the center span is 50 feet. Concrete curbs along the deck edges yield a clear roadway width of 31.5 feet. The roadway consists of two 12 foot lanes with 3 foot shoulders.

The original construction of the southern section was done in 1934 and a widening to the northern side was performed in 1968.

The foundations are mass-gravity type. The older part of substructure is built of granite masonry units connected with cement mortar. In the new section, the bottom part of the foundation is made of unreinforced concrete and the top part – of masonry. All piers and abutments are founded directly on the bedrock.

The deck is supported by seven steel I-beam girders. Four of them derive from the original construction and three from the second construction stage. The girders differ with cross-section dimensions. Each of them is divided into three parts and use a pin-and-hanger system at the expansion joints. They rest on steel bearings. Stiffness in the transversal direction is ensured by 2 rows of C-beams and 6 rows of I-beams. The connections between beams are bolted and/or welded. The deck is built of reinforced concrete, covered with a layer of asphalt pavement. In the original design the thickness of the reinforced concrete deck differs from 7in at the curbs to 8in at the centerline. The thickness of the new section is constant and equal to 7in. Metal railing is mounted to the side of the deck and external girders.

The main alterations to the original structure include: removal of portions of the abutment concrete bridge seat and abutment masonry wingwalls, removal of part of the masonry at the top of the piers, removal of the right side of the concrete curb. The existing concrete was roughened on the joint planes and epoxy adhesive was applied immediately before placing new concrete. Holes are drilled in existing slab and dowels are grouted in. This kind of treatment ensures good adherence of both sections.

The topography of the terrain is characterized by gently undulating surface underlain by bedrock, which consists of limestone and calcareous shale. The bedrock is overlain by granular material (sand and gravel). The layer's thickness is approximately 10ft at the abutments and about 4ft around the piers. The seismic zone for this region is established as Zone 1, therefore seismic effects are not an issue.

2. Description of the Computational Model

Preparation of a good numerical representation of any structure requires a significant amount of information. Most of it was adopted from as-built drawings and also field and laboratory tests. Some assumptions had to be made with regard to material properties not covered by the tests.

The computational model of the structure consists of ~190,000 four-node and three-node shell finite elements, ~50,000 solid elements (both, hexahedral and tetrahedral with the latter used mainly for mesh transition zones) and 14 beam elements. This sums up to a number of nodes of about 260,000. Mesh density is based on previous experiences with structural modeling. Sixteen materials were modeled with the use of five different material models. To take into account regions of different thickness, material etc., 37 sections and 14 composite parts were distinguished. Rigid link finite elements were used to join parts of the model.

2.1. The substructure

2.1.1. Geometry

The geometry of the model was based on as-built drawings and surveying data. The input from the drawings was correlated with more up-to-date data from on-site measurements. The provided coordinates defining the three-dimensional shape of masonry structures and the topography of the terrain were used to prepare the model in LS-PrePost [1].

Figure 2.1 shows as-built drawings from 1934 with latter corrections from 1966 (in red) of side and top views of Lake Mary Road Bridge. Figure 2.2 presents an isometric view from south of the bridge foundations. Concrete parts are shaded in grey to distinguish them from masonry sections. Joint lines between old and new structures are also shown. Approximate locations of eight boreholes drilled in the foundations and one in the road are presented, along with approximate ground and bedrock levels. The supports are signed: Abutment 1 - Ab1, Pier 1 - P1, Pier 2 – P2, Abutment 2 – Ab2. These acronyms will be used throughout the report.

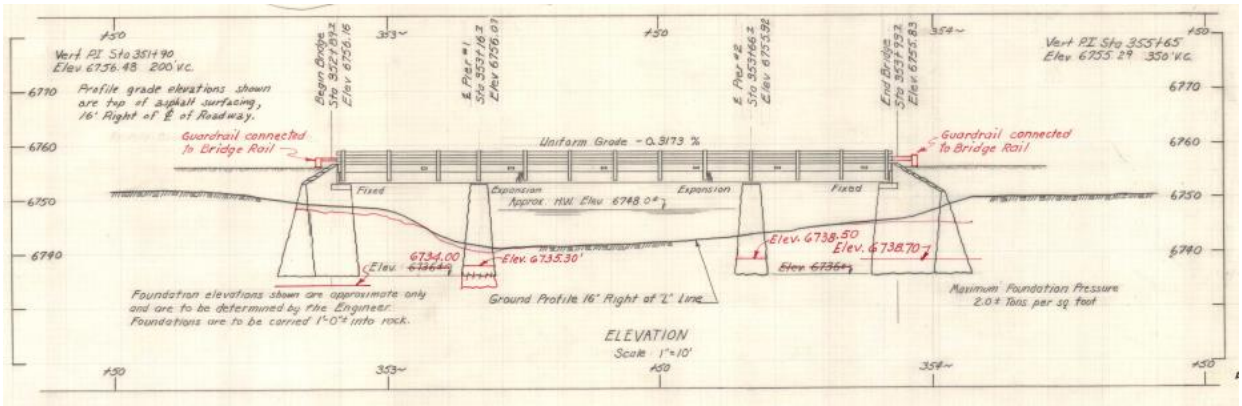

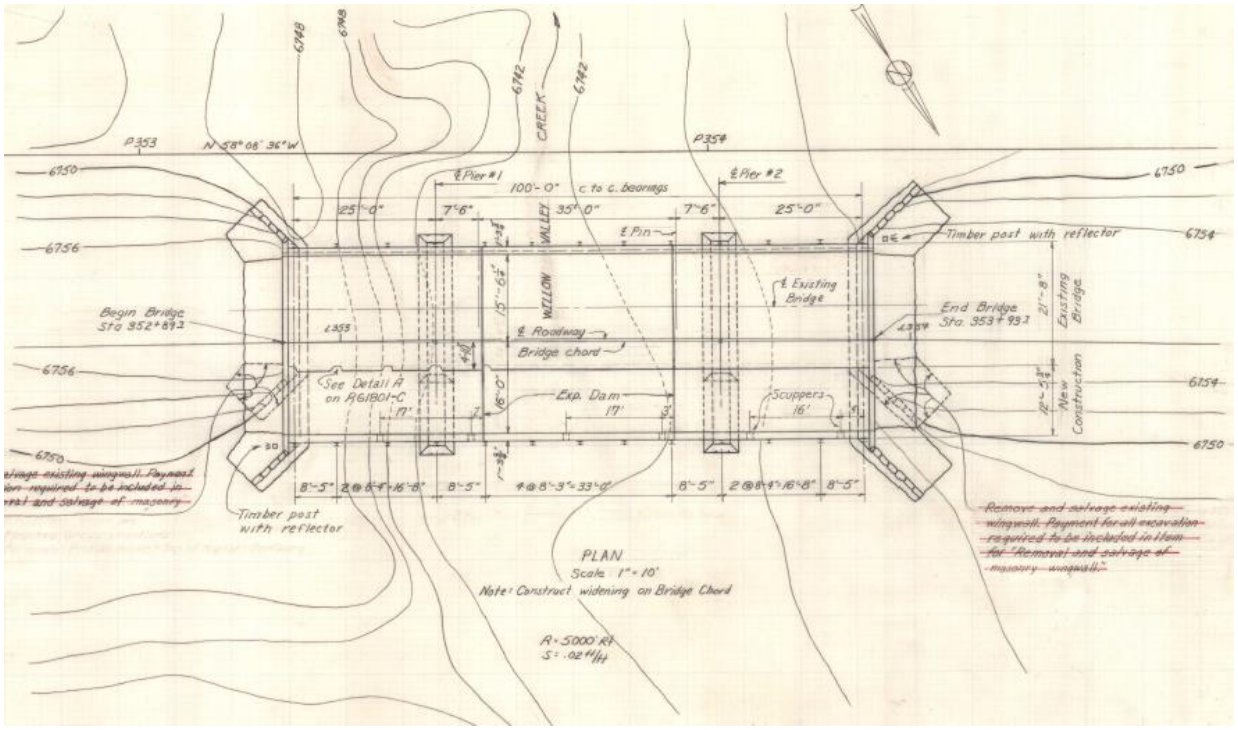

Figure 2.1: Side and top views of Lake Mary Road Bridge. Source: As-built drawings from 1934 with latter corrections from 1966

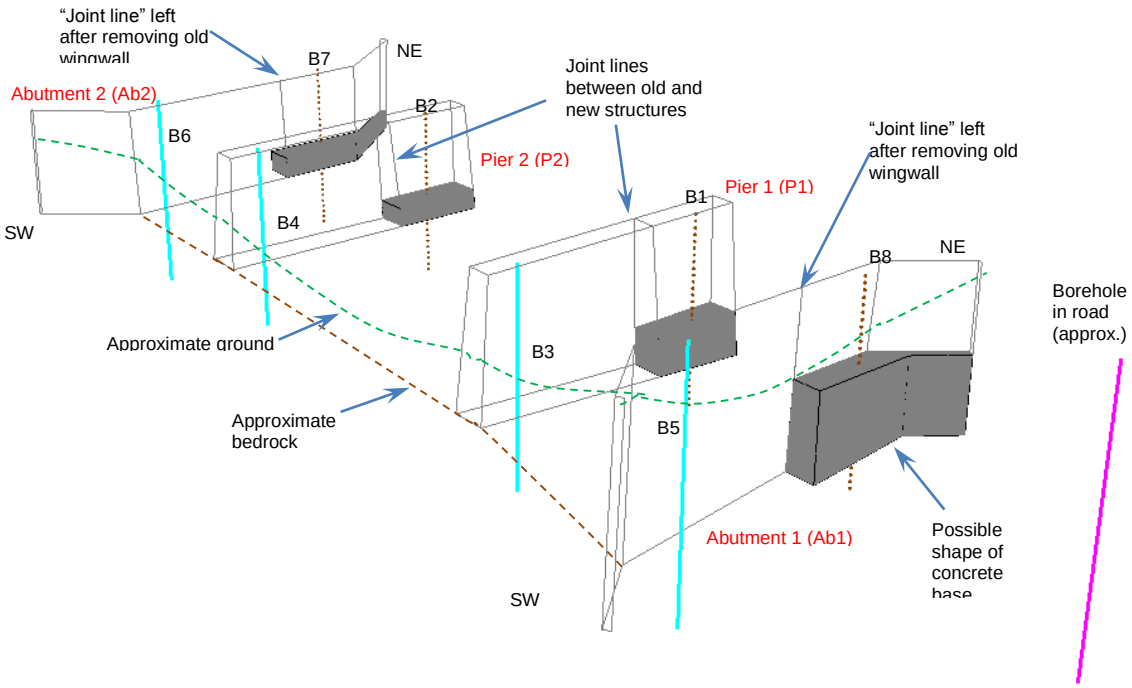

Figure 2.2: Isometric view from south of the bridge foundations (source: arizonasurveying.com)

2.1.2. Material properties and material models

The types of structural materials and their properties used in the superstructure were obtained from the as-built drawings. Borings done in the piers and abutments provided data on materials used in the foundations, soil and bedrock. Laboratory tests were done on the recovered samples.

The property values of masonry and concrete were established for a sample from the newer section of the foundations. A solid granite masonry unit was tested for mechanical properties. The sample didn't include the cement mortar which bonds the units together. Therefore a comparative analysis was done to assess the influence of the lower strength of mortar on the overall response of the bridge. Cases of 100%, 80% and 60% of strength and stiffness were used in a set of numerical simulations. It must be emphasized that this is a simplified method and was chosen due to lack of more detailed data on the crack location and distribution. More elaborate laboratory tests are needed in order to develop a more accurate model, which could better predict failure of the structure.

Moreover, the on-site tests revealed that the old part has some small debonds between stones. For this reason, it was decided to decrease the values of stiffness and strength of masonry by 20% for that region. Failure of the materials was not included in the models.

Material properties, obtained from as-built drawings, laboratory tests or assumed based on the literature, are shown in Table 1.

LS-DYNA offers a variety of concrete material models [2], which differ with the level of sophistication. Three of them were chosen for comparison. Only so called 'simple input' models were considered, which allow the user to input a full set of experimentally determined properties or generate a set of properties from basic input.

a) MAT072R3 – a three-invariant model, which uses three shear failure surfaces; it allows for model parameter generation, based solely on the unconfined compression strength of the concrete,

b) MAT084 – Winfrith material model, which is a smeared crack and smeared rebar model; implemented in the 8-node single integration point continuum element,

c) MAT159 (CSCM) – a three-invariant model with a continuous intersection between shear yield surface and hardening cap.

The parameter values needed for the mentioned models were taken from literature (C. Bojanowski, M. Balcerzak, Modeling of Reinforced Concrete Slab Subjected to Explosive Loading Using Simple Input Concrete Models in LS-DYNA).

A linear elastic - perfectly plastic material model (MAT024 - MAT_PIECEWISE_LINEAR_PLASTICITY) was also taken into consideration.

Table 1: Material properties

Concrete		
Specified compressive strength	3300 psi	22.75 MPa
Tensile strength	493 psi	3.4 MPa
Elastic modulus	$3.0 \cdot 10^3$ ksi	21 GPa
Unit weight	150 $\frac{lb}{ft^3}$	2400 $\frac{kg}{m^3}$
Reinforcing steel		
Elastic modulus	$30 \cdot 10^3$ ksi	210 GPa
Yield strength	$40 \cdot 10^3$ psi	276 MPa
Tensile strength	$70 \cdot 10^3$ psi	483 MPa
Structural steel		
Yield strength	$36.3 \cdot 10^3$ psi	250 MPa
Tensile strength	$58 \cdot 10^3$ psi	400 MPa
Granular overburden		
Unit weight	125 $\frac{lb}{ft^3}$	2000 $\frac{kg}{m^3}$
Friction angle	32°	
Limestone /calcareous shale		
Rock Quality Designation	95	
Unit weight	187 $\frac{lb}{ft^3}$	3000 $\frac{kg}{m^3}$
Poisson's Ratio	0.23	
Modulus	$5.7 \cdot 10^3$ ksi	39.3 GPa
Compressive strength	$8.5 \cdot 10^3$ psi	58.6 MPa
Concrete		
Unit weight	150 $\frac{lb}{ft^3}$	2400 $\frac{kg}{m^3}$
Poisson's ratio	0.15	
Modulus	$3.6 \cdot 10^6$ psi	24.8GPa
Compressive strength	$4.0 \cdot 10^3$ psi	27.6 MPa
Granite-faced masonry		
Unit weight	160 $\frac{lb}{ft^3}$	2560 $\frac{kg}{m^3}$
Poisson's ratio	0.20	
Modulus	$7.6 \cdot 10^3$ ksi	52.4 GPa
Compressive strength	$8.0 \cdot 10^3$ psi	55 MPa

In preliminary analyses the existing structural load was applied to check the foundation's response. It showed that the results were very similar in each of the four cases, including the elasto-plastic material model. That indicates that the substructure behavior is elastic. Therefore, the simplest model could be used. Computational performance was also considered and finally material model MAT084 was chosen as it gave the shortest computational time (which was 11 h 47 min, comparing to: MAT024-13 h 26 min, MAT072R3-15h 35 min, MAT159-16 h 51min on 32 CPUs, using LS-DYNA version: mpp971d R5.0).

Information on masonry properties was limited. Only general characteristics were provided, including modulus, compressive strength and Poisson's ratio, therefore the simplest elastic - perfectly plastic material model was used - MAT025. More advanced models, allowing for modeling cracks or considering the composite nature of masonry, require more input data, which could only be obtained from additional laboratory tests.

The sample recovered from one of the boreholes and tested by geotechnical engineers consisted of pure rock (it didn't include mortar). It is known that masonry composed of masonry units and mortar has smaller stiffness and strength than the rock itself [3]. For this reason, the influence of decreased property values on the overall behavior of the structure was examined. Two cases were considered, in which strength and stiffness of masonry were equal to 60% and 80% of the original values. Displacements of selected points were compared and it was found that the differences were small – the difference between analyzed cases wasn't larger than 0.1 mm. Figure 2.3 presents the vertical displacements of six points along the center of the midspan for 100%, 80%, and 60% of assumed masonry strength and stiffness. The largest displacements were registered at point 6, laying between the last two girders on SW side, and were in the range of 5 mm. Figure 2.4 shows vertical displacements of points on the top surfaces of the foundations for 100%, 80%, 60% of assumed masonry strength and stiffness on both abutments and piers. As it was expected, the changes in displacements of the old part of the pier are greater than for the newer part. In this region, the influence of lower stiffness is less significant.

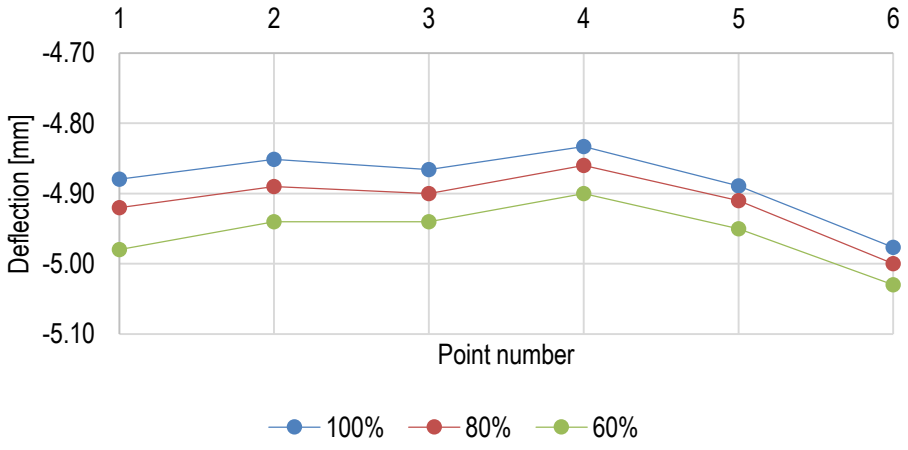

Figure 2.3: Vertical displacements of six points along the center of the midspan for 100%, 80%, 60% of assumed masonry strength and stiffness

a)

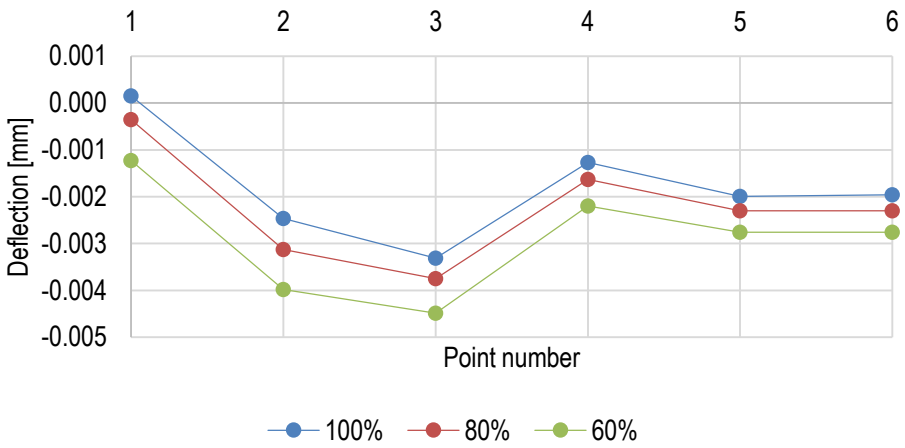
1
2
3
4
5
6
0.001
0.000
-0.001
-0.002
-0.003
-0.004
-0.005
Deflection [mm]
Point number
100%
80%
60%

b)

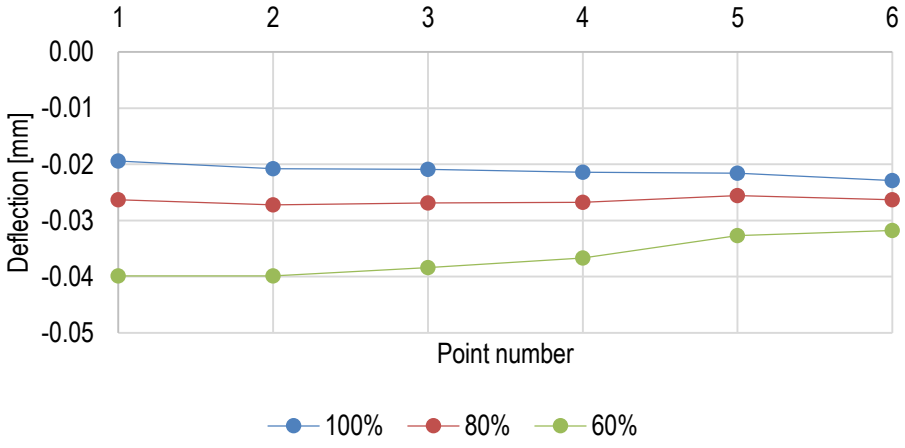
1
2
3
4
5
6
0.00
-0.01
-0.02
-0.03
-0.04
-0.05
Deflection [mm]
Point number
100%
80%
60%

c)

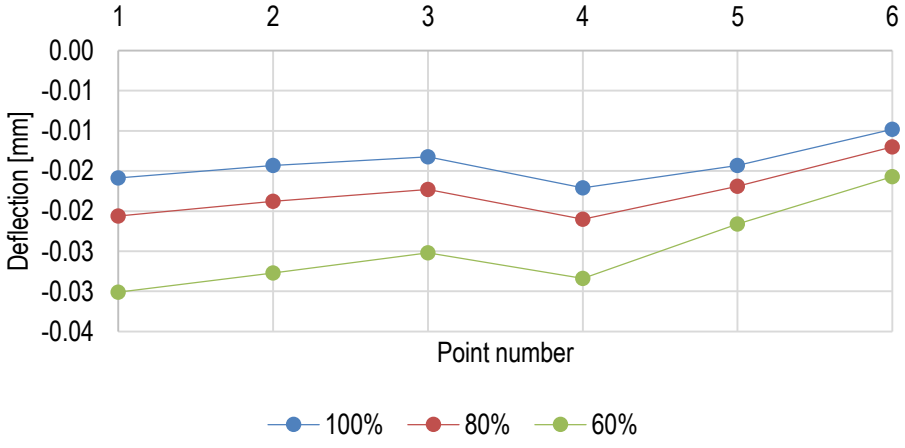
1
2
3
4
5
6
0.00
-0.01
-0.01
-0.02
-0.02
-0.03
-0.03
-0.04
Deflection [mm]
Point number
100%
80%
60%

d)

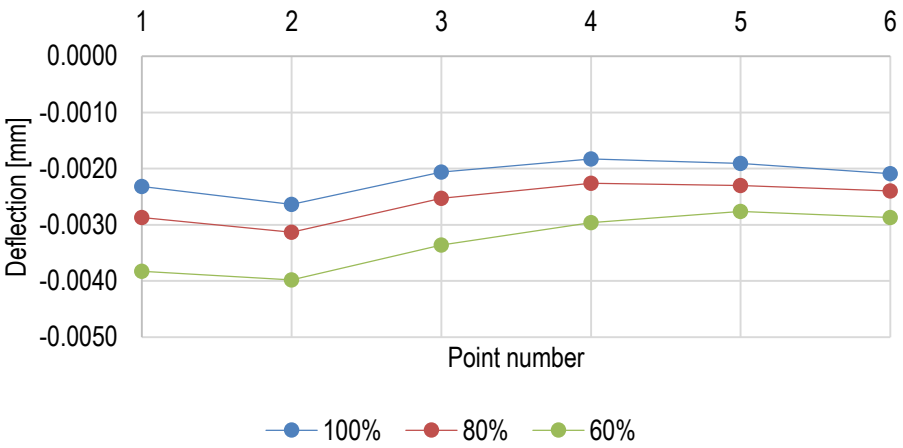

Figure 2.4: Vertical displacements of points on the top surfaces of the foundations for 100%, 80%, 60% of assumed masonry strength and stiffness on: a) Abutment 1, b) Pier 1, c) Pier 2, d) Abutment 2

2.1.3. Boundary conditions

In two of the considered models, granular overburden is modeled as distributed load acting on the foundations. Pore water pressure is included in the calculations. The ground levels around the foundations were established approximately from surveying data from the known locations of the lowest source and receiver points on the surface of each foundation, which were about 6 inches above the ground.

The granular overburden load is divided into vertical and horizontal components. In LS-DYNA only normal and tangential loads can be applied to finite element faces. The foundation walls are inclined to the horizontal direction at different angles, therefore normal and tangential forces have to be calculated. Figure 2.5 shows an infinitesimal element in static equilibrium. Vertical and horizontal earth loads are transferred as pressure and traction on the foundation walls.

At depth z we get

$$\sigma_v = \gamma z,$$

$$\sigma_h = K_0 \sigma_v + \mathrm{u}\,,$$

where: σ_v – vertical component of earth pressure, σ_h - horizontal of earth pressure, pore water pressure $u = 9.81 \frac{kN}{m^2}$, coefficient of lateral earth pressure $K_0 = 1 - \sin\phi = 0.47$, γ – soil unit weight.

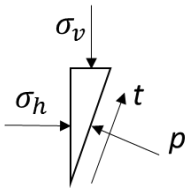

Figure 2.5: Static equilibrium of an infinitesimal element

Pressure acting on the walls is equal to

$$p = \sigma_h \cos\alpha + \sigma_v \sin\alpha$$

and traction can be calculated as

$$t = -\sigma_h \sin\alpha + \sigma_v \cos\alpha,$$

where: $\sin\alpha = \frac{5}{13}$, $\cos\alpha = \frac{12}{13}$.

LS-DYNA doesn't allow linearly changing distributed load on irregular surfaces, therefore a simplification had to be made. The loaded region was divided along the vertical direction and average load values, increasing with depth, were assigned.

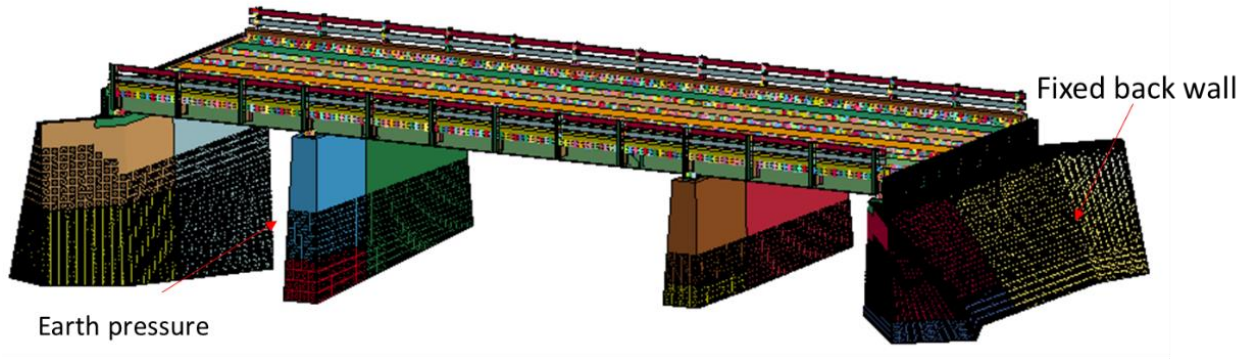

Figure 2.6: Boundary and loading conditions on the bridge foundations

A study of fixed vs. free boundary conditions on the back walls of the abutments was conducted. The interaction between the walls and surrounding bedrock and granular soil is not known, as no tests were performed on-site. Therefore two extreme cases were analyzed, to cover a range of possible behaviors. Different boundary conditions were depicted on Figure 2.6. In the first one, all nodal displacements are constrained. This makes the structure stiffer, as it limits the possible deformations. In the second, the walls are loaded by the earth pressure and there is no limitation on the displacements, therefore the substructure is less stiff.

The limestone bedrock, which supports the substructure, is modeled in two ways. Most of the analyses consider the bedrock as fixed boundary conditions applied to the nodes on the bottom surfaces of the foundations. This choice was determined by the condition of the rock

specimen retrieved from the site and no apparent voids between the foundation and underlying bedrock. The Rock Quality Designation (RQD), which is an index of rock quality, was established by geologists to be equal 95. RQD measures the percent of core recovery and this value indicates that the rock mass quality is excellent.

As a reference, an analysis was performed with the bedrock and overburden modeled explicitly, with solid finite elements. The geometry of the new model is presented on Figure 2.7. The additional 320,000 of solid finite elements make the simulation more time consuming and double the computational time.

Parts that represent the soil have material properties of the granular overburden and limestone gathered in Table 1. The boundary conditions used are as follows: on the bottom surface constraints on the vertical displacements are set, on the side walls – horizontal displacement components are constrained.

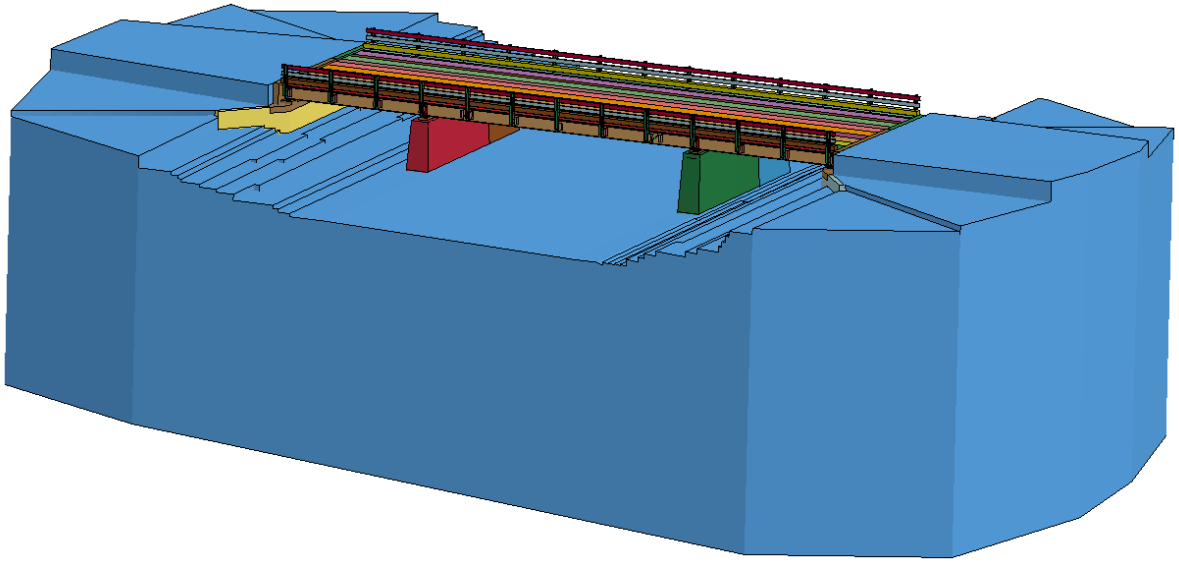

Figure 2.7: A general view of the model with overburden and soil

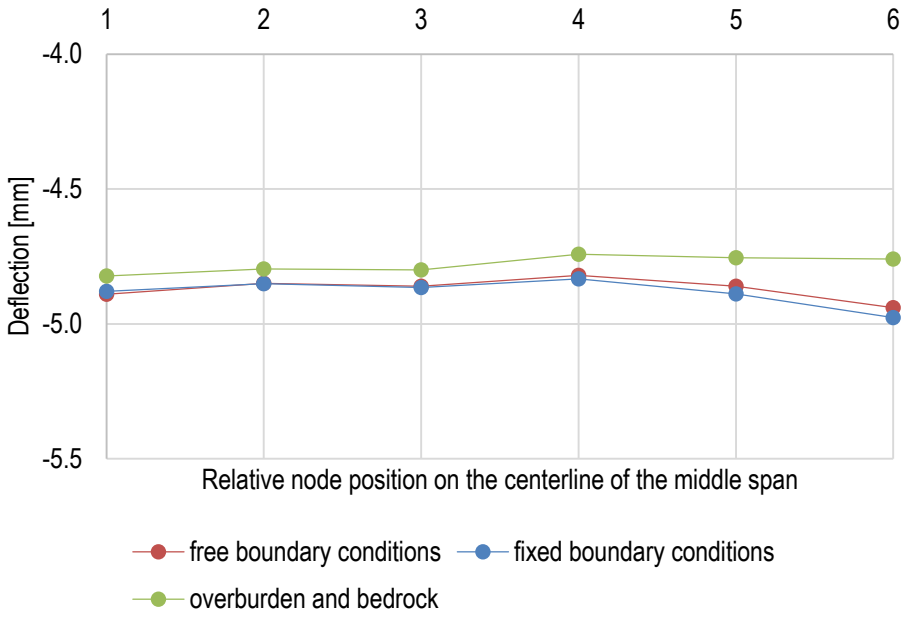

Figure 2.8: Vertical displacements of six points along the center of the midspan for free and fixed boundary conditions on the abutment back walls as well as explicitly modeled overburden and bedrock

a)

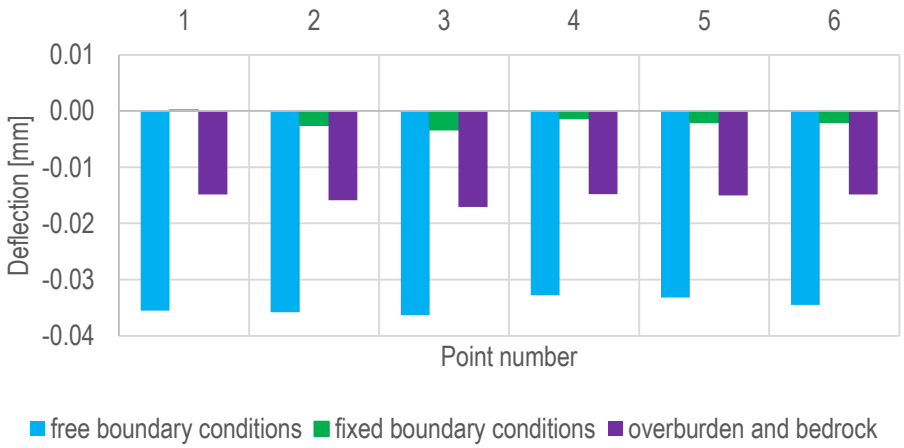

b)

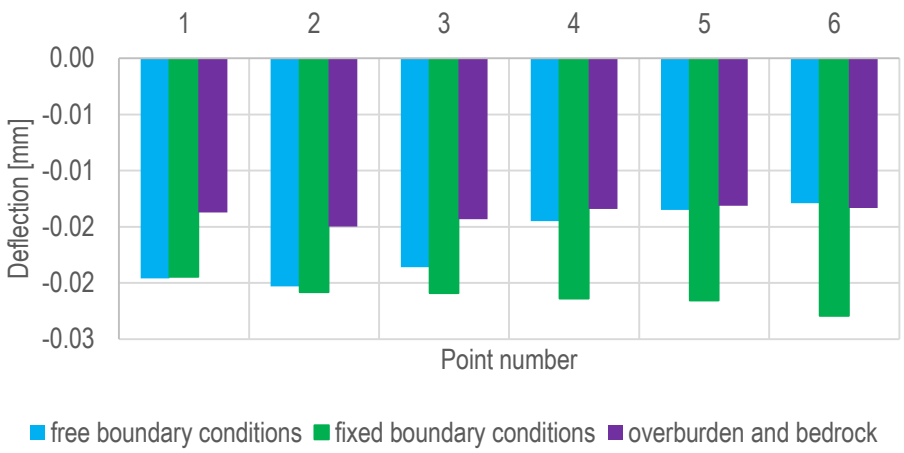

c)

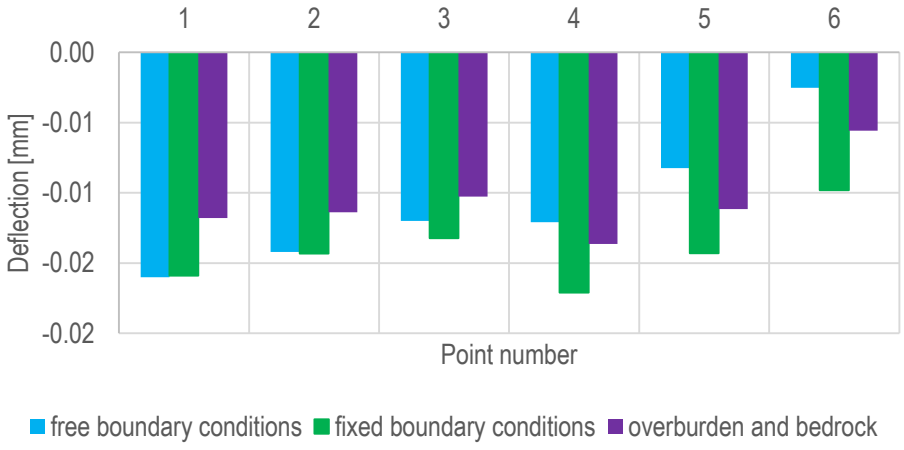

d)

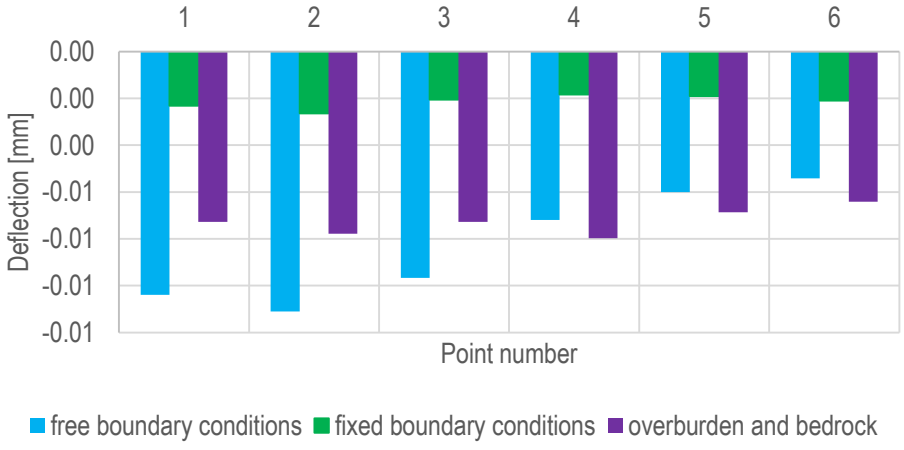

Figure 2.9: Vertical displacements of points on a) Abutment 1, b) Pier 1, c) Pier 2, d) Abutment 2 for free and fixed boundary conditions on the abutment back walls as well as explicitly modeled overburden and bedrock

Comparison of the response, including displacements and stress distribution, was done for these three cases and shown on Figure 2.8 and Figure 2.9. Figure 2.8 covers the changes of vertical displacements of six points along the center of the midspan for fixed and free boundary conditions as explicitly modeled overburden and bedrock. Figure 2.9 presents the vertical displacements of points on Abutment 1, Pier 1, Pier 2 and Abutment 2.

The extended model gives the lowest deflections of the deck. The differences are small, the highest is about 0.12mm, which gives about a 2% relative error. The maximum deflections of the foundations (at points on top surfaces of the supports) are higher for abutments in free boundary conditions case and for piers in fixed boundary conditions case. The extended model gives results that fall in between the other models. This difference is mostly caused by the way the overburden is modeled. In the first case, it is considered as a distributed load acting on the piers, which gives a more flexible response of the supports. In the second, it is represented with solid finite elements that share nodes with the finite elements forming the piers. In this case the structure is stiffer. The extended model gives the most even displacements, because all foundations share nodes with the soil and bedrock.

2.2. The superstructure

2.2.1. Geometry

The deck is made of reinforced concrete with a top layer of asphalt. Instead of using solid elements and modeling the reinforcement, concrete, and asphalt layers explicitly, the deck was modeled with so called composite shell elements (with the use of *PART_COMPOSITE option) that allow definition of various layers of materials along the element's thickness. That means that one layer of shell finite elements is enough to represent a complicated reinforced concrete slab. The reinforcement consists of two layers of lateral and transverse reinforcement, on the bottom and top of the slab. The density and layout of the transversal reinforcement differs in the regions above girders and in between them. In the first case there are more bars in the top layer, in the second – in the bottom layer. Lateral bars are almost uniformly laid out. Moreover, slab thickness varies along the transverse direction. As LS-DYNA allows definition of parts of uniform thickness and number of layers, fourteen sections were distinguished along the width of the deck, which differ with: number of layers and their thicknesses and also percentage of reinforcement.

2.2.2. Material properties and material models

Reinforced concrete was represented with EC2 material model *MAT172, whose behavior is defined by simple input parameters and empirical equations from Eurocode 2. This material model can represent plain concrete only, reinforcing steel only, or a smeared combination of concrete and reinforcement. This model includes concrete cracking and crushing and also reinforcement yield, hardening and failure.

Structural steel was modeled with elastic-perfectly plastic material *MAT024 (material properties are given in Table 1) and asphalt – with viscoelastic material model *MAT006. Material properties of asphalt were assumed as: unit weight $172\frac{lb}{ft^3} = 2750\frac{kg}{m^3}$, bulk modulus $K =$

$566ksi = 3.9GPa$, short-time shear modulus $G_0 = 188ksi = 1.3GPa$, long-time shear modulus $E_c = 75.4 \cdot 10^3 psi = 520MPa$, decay constant $\beta = 0.006$.

The slab was tied to the beams with rigid links (*CONSTRAINED_NODAL_RIGID_BODY - CNRB), instead of sharing nodes. They provide necessary connection between the parts and give a possibility of taking into account thicknesses of the slab and the girder top flange.

The hangers in the pin-hanger system in the expansion joints were simplified. The hangers were represented by truss finite elements with appropriate cross-sectional area and material properties.

Steel beams were modeled with shell finite elements. The dimensions of the beams were assumed according to as-built drawings. The connections between beams are not modeled explicitly. It was assumed that the connections are fixed and therefore the beam ends share common nodes. The simplification made during the modeling have been shown on Figure 2.10.

The curbs, as they are more bulky then the rest of the slab, were modeled with solid elements and tied to the slab with rigid links, see Figure 2.11.

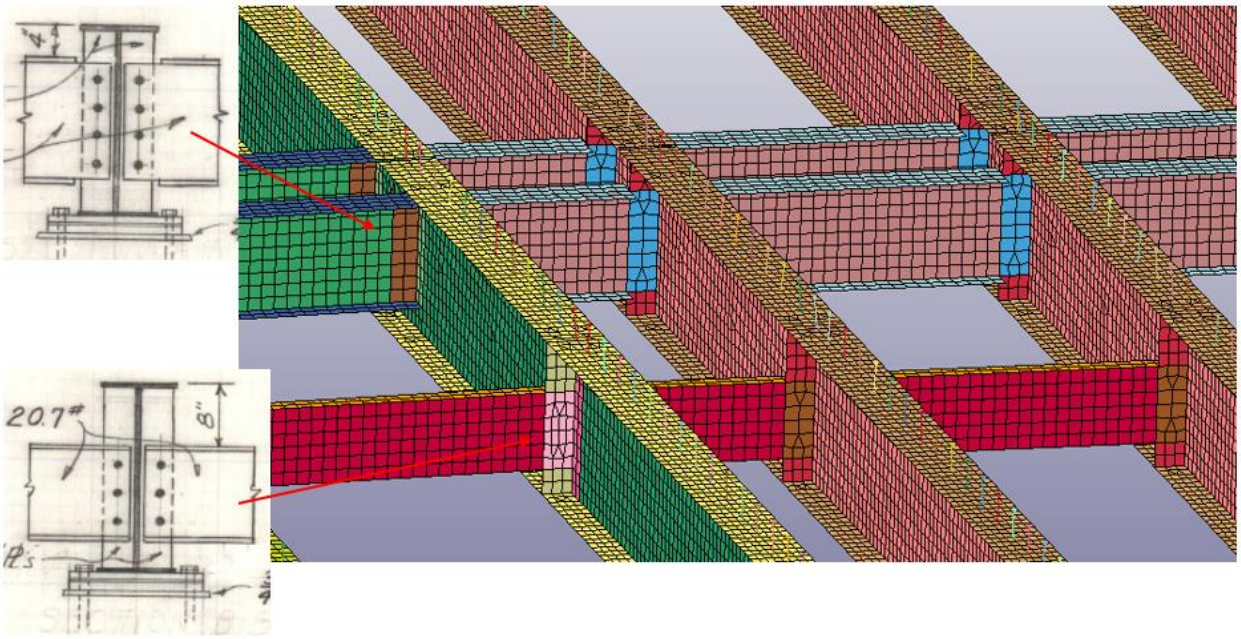

Figure 2.10: Details of structural modeling

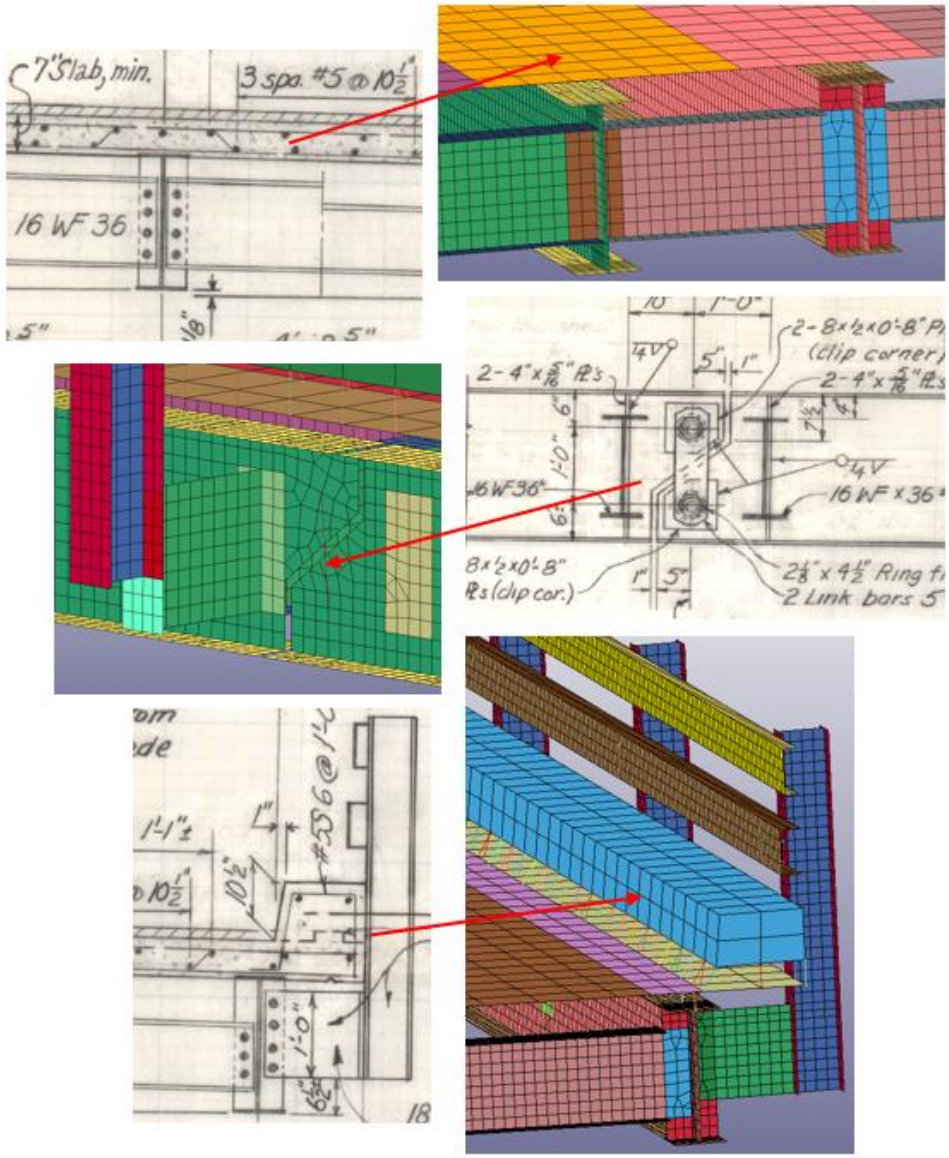

Figure 2.11: Details of structural modeling, cont'd

3. Analysis methods

Several analysis methods were considered in the present study. The behavior of the bridge due to static, dynamic and impact loads was examined.

Static tests include:

a) an increase of the existing structural load, as it is anticipated that the Willow Valley Bridge will be rehabilitated and the superstructure will be replaced and a wider one,

b) design live load from a HS20-44 truck at chosen critical positions and design lane load.

Dynamic tests cover runs of a Mack CH613 truck tractor in four different positions on the bridge, all at the same limit speed for Lake Mary road.

In each loading case the vertical displacements were recorded:

a) on the superstructure at the centerline of the middle span

b) on the top surface of the substructure

In the case of impact tests, several impact load magnitudes were taken into account and applied at various points on the substructure. A possibility of using these tests in structural monitoring was examined. Accelerations were measured in a chosen set of points.

The quantities chosen for comparison in different loading cases are vertical displacements and equivalent von Mises stress. The deflections of the centerline of the deck middle span were recorded in six points, marked D1 to D6 in Figure 3.2. The foundations are analyzed more thoroughly. The naming convention for supports is shown in Figure 3.1. Vertical displacements are checked at several points on top surfaces of both abutments and piers, where the values are expected to be the highest. Six output points were chosen in between the girders and named Ab1-1 to Ab1-6 for Abutment 1, P1-1 to P1-6 for Pier 1, P2-1 to P2-6 for Pier 2 and Ab2-1 to Ab2-6 for Abutment 2. They are presented in Figure 3.3.

The Von Mises formula for combining the principal stresses into an equivalent stress is used. This value is then compared to the yield stress of the material. If the von Mises stress exceeds the yield stress, then the material is considered to be at the failure condition. Locations of maximum von Mises stress in the foundations were found and compared to their structural capacity. The stress distribution at the places where borings were done was calculated to allow comparison with data from sensors planned to be mounted in the openings. The location of the cross-sections for which contour plots were recovered is shown in Figure 3.1. Max values of stresses on the bottom surfaces of the foundations were also compared to load carrying capacity of the bedrock.

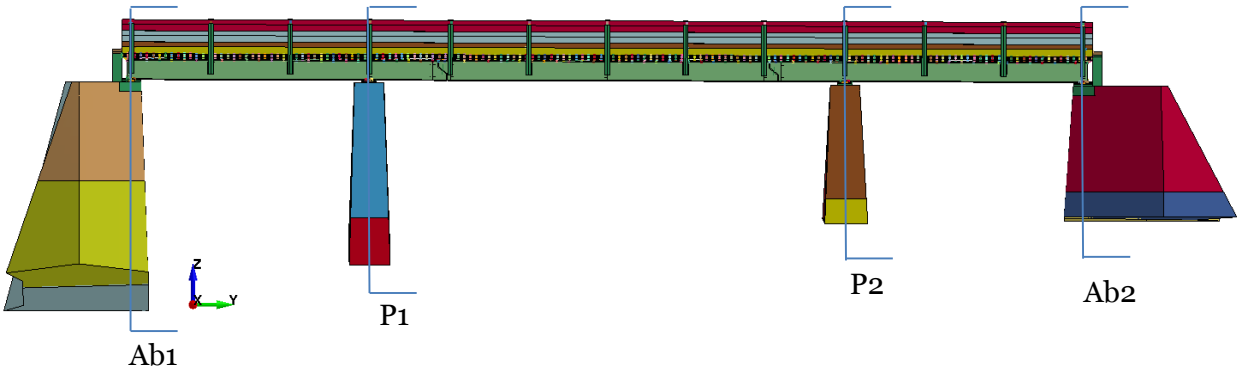

Figure 3.1: Naming convention for the supports: Ab1 – Abutment 1, P1 - Pier 1, P2 - Pier 2, Ab2 - Abutment 2 and locations of cross section planes through foundations.

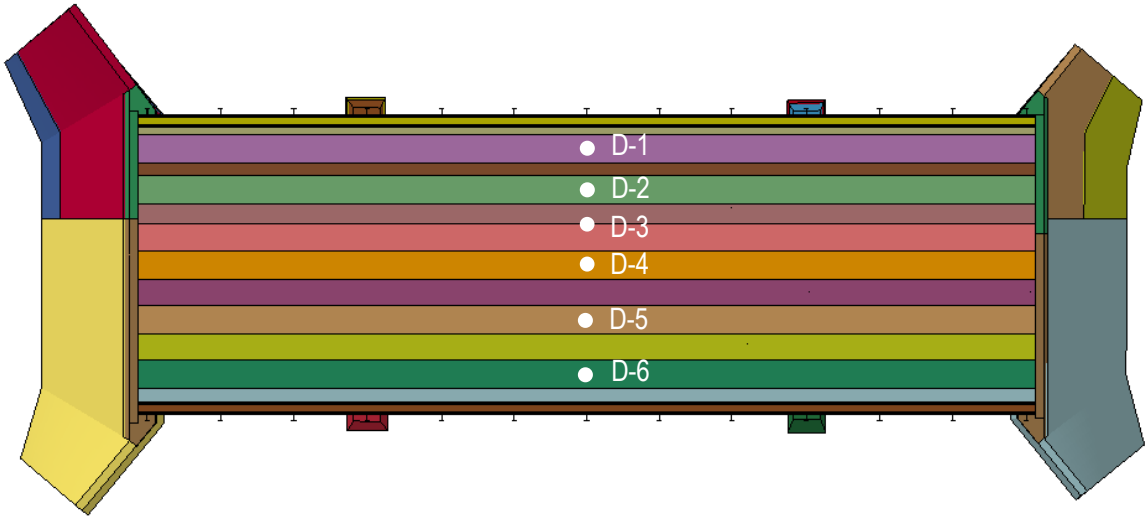

Figure 3.2: Locations of output nodes on the deck

a)

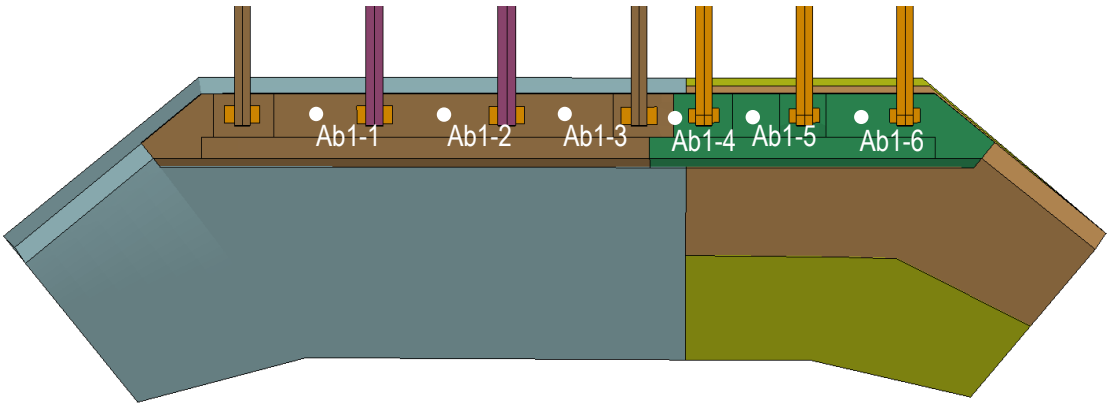

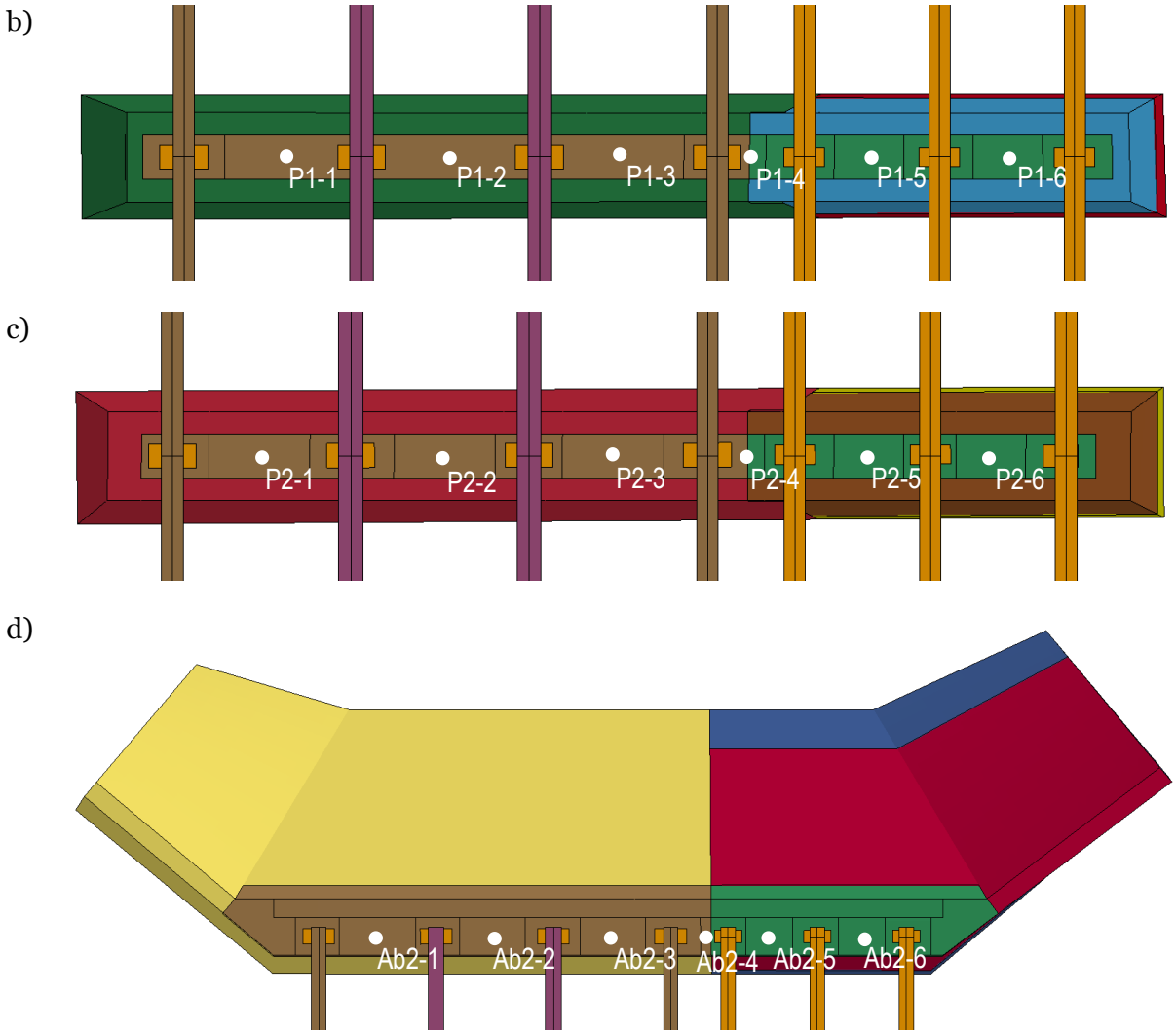

Figure 3.3: Output nodes on the top surfaces of the foundations a) Abutment 1, b) Pier 1, c) Pier 2, d) Abutment 2

The recommendations of Load and Resistance Factor Design (LRFD) design were taken into consideration in structural calculations. Strength limit state Strength I of the bridge was examined, which is a basic load combination that relates to the normal bridge use without wind effects [4].

Basic LRFD design equation is

$$\sum \eta_i \gamma_i Q_i \leq \phi R_n \qquad [1]$$

where $\eta_i = 1$, γ_i is the load factor, ϕ is the resistance factor, Q_i is the nominal force, and R_n is nominal resistance.

Load factor values are: 1.25 for dead load; 1.75 for live load, horizontal earth pressure: 1.50 when active, 1.35 when at-rest, 1.30 for vertical earth pressure for rigid buried structure; an

average of 1.5 was adopted in the calculations. In geotechnical stability analyses a load factor equal to unity ($\gamma = 1$) is used. The resistance factor for spread footings built on rock equals 0.45 [5].

3.1. Increase of structural load

The first loading case takes into account the plans to replace the existing superstructure with a wider, and therefore heavier, deck. The foundations will have to support additional load, which is not yet known, as the design is not completed. To simulate this new situation, the existing conditions of the superstructure are adapted to represent the change in the design. This allows the response of the foundations to the increased structural load to be evaluated. The resulting increase in weight is expressed by an additional uniform distributed vertical load and is applied to the deck surface in amounts equal to 10%, 20% and 30% of the existing superstructure weight.

The points on the deck, at which vertical displacements were recorded, lay in between girders. The choice is based on the assumption that these are the locations of the highest deflections. It can be clearly seen that the deck deforms in an elastic manner – the deflections increase linearly with the increase of the additional structural load. Maximum deflection doesn't exceed 7.5 mm for the third load case. Vertical displacements of chosen points on the deck due to increase of structural load by 10%, 20% and 30%, can be seen in Figure 3.4.

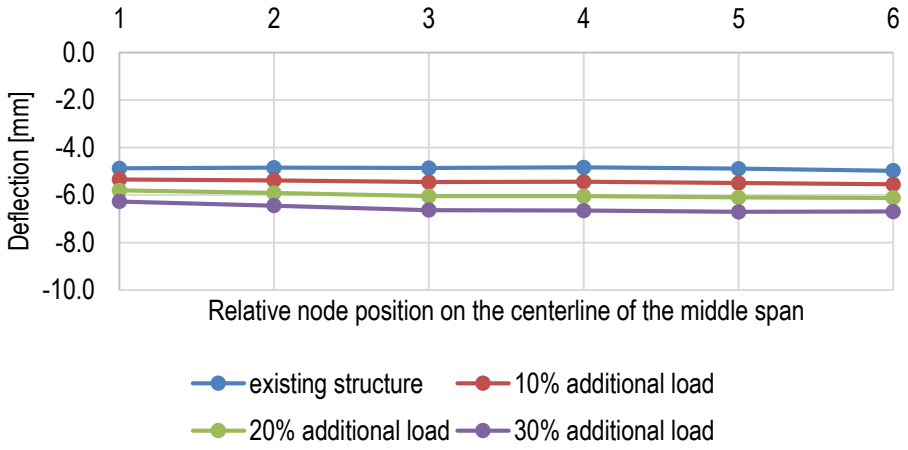

Figure 3.4: Vertical displacements of points D-1 to D-6 on the deck due to increase of structural load by 10%, 20% and 30%

The displacements of the foundations are a few orders of magnitude smaller than the ones observed on the deck. Figure 3.5 shows vertical displacements of a chosen set of points due to increased structural load on both abutments and piers. The changes due to increased load are small. Piers are more flexible than the abutments and therefore show larger deformations. If onsite measurements are planned, placing sensors on their top surfaces is recommended.

a)

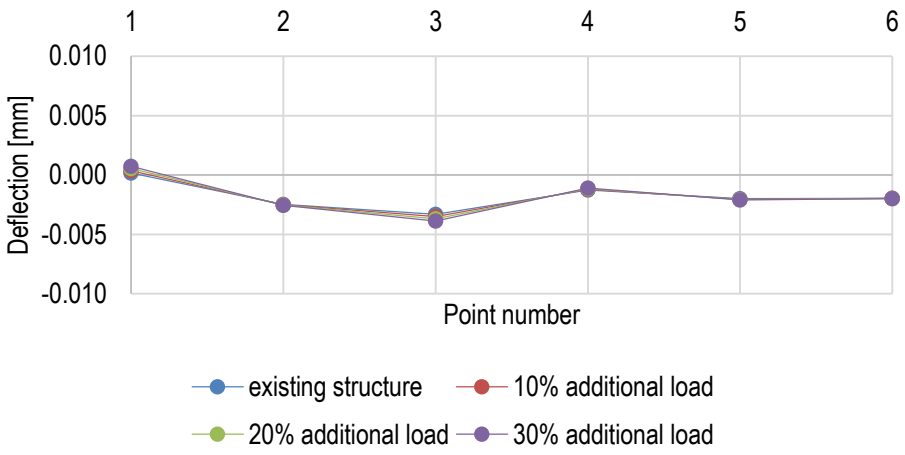
1
2
3
4
5
6
0.010
0.005
0.000
-0.005
-0.010
Deflection [mm]
Point number
existing structure
10% additional load
20% additional load
30% additional load

b)

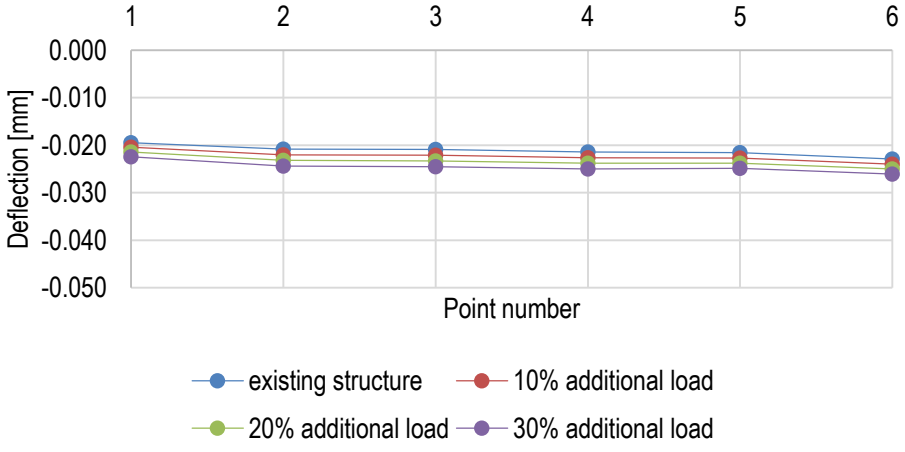
1
2
3
4
5
6
0.000
-0.010
-0.020
-0.030
-0.040
-0.050
Deflection [mm]
Point number
existing structure
10% additional load
20% additional load
30% additional load

c)

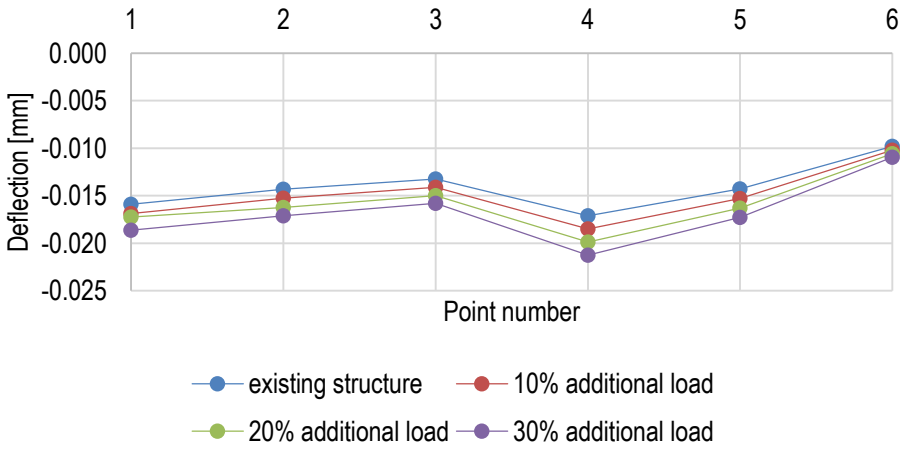
1
2
3
4
5
6
0.000
-0.005
-0.010
-0.015
-0.020
-0.025
Deflection [mm]
Point number
existing structure
10% additional load
20% additional load
30% additional load

d)

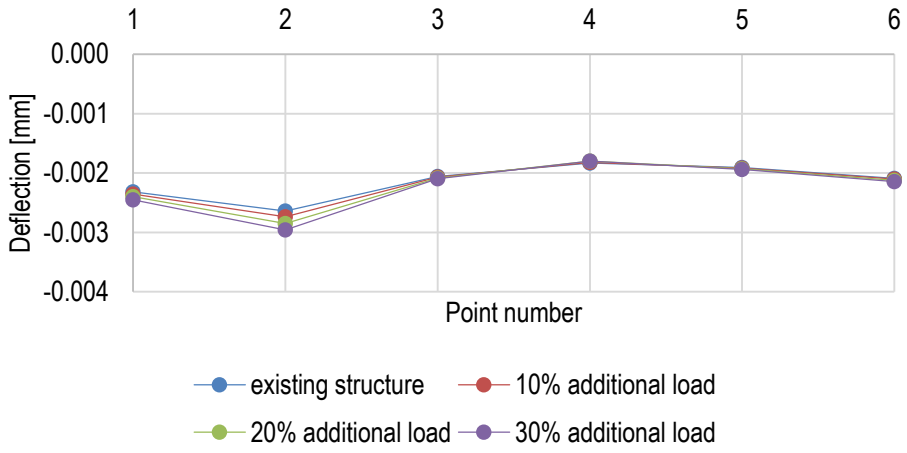

Figure 3.5: Vertical displacements of a chosen set of points due to increased structural load; a) Abutment 1, b) Pier 1, c) Pier 2, d) Abutment 2

The highest values of equivalent stress are located at the bottom of the older part of Pier 1, close to the joint plane. An example contour plot for the load case of 30% additional load was shown in Figure 3.6. Red areas represent the highest values and blue areas the lowest values of equivalent stress. Comparing the stress values to structural and geotechnical capacity, gives the percentage of used capacity (presented in Table 2). The highest usage, for 30% of additional load, equals 4% and 2.4% of, accordingly, structural and geotechnical capacity. The calculations were performed according to Equation 1. Stress concentration locations are also apparent below the bearings. Load cells can be mounted in these sections.

Figure 3.7 to Figure 3.9 show contour plots of von Mises stress on the cross-section planes going through the locations of the boreholes. Placement of load cells in the drilled openings is planned, therefore it's worth checking what values and stress distribution can be expected there.

Table 2: Maximum values of von Mises stress in the foundations due to increased structural load

Percent of additional load	**0%**	**10%**	**20%**	**30%**
Mises stress [MPa]	0.528	0.566	0.603	0.641
Percentage of used structural capacity	3.3%	3.6%	3.8%	4.0%
Percentage of used geotechnical capacity	2.0%	2.1%	2.3%	2.4%

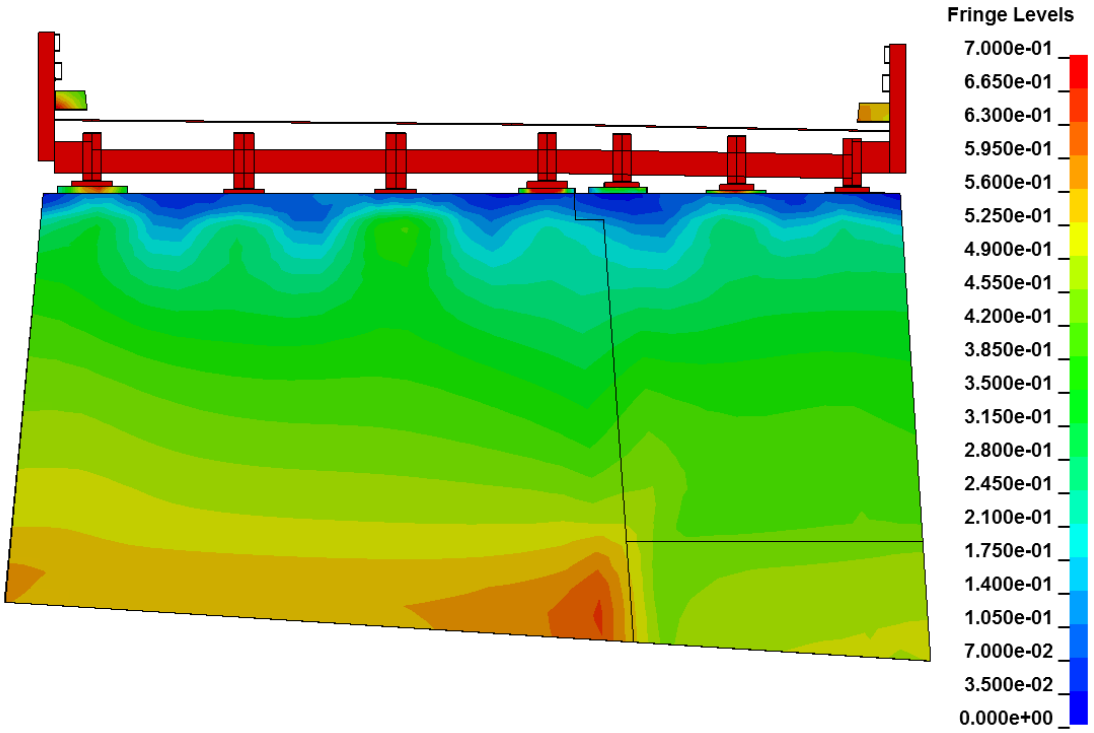

Figure 3.6: A contour plot of von Mises stresses in Pier 1 for 30% additional structural load

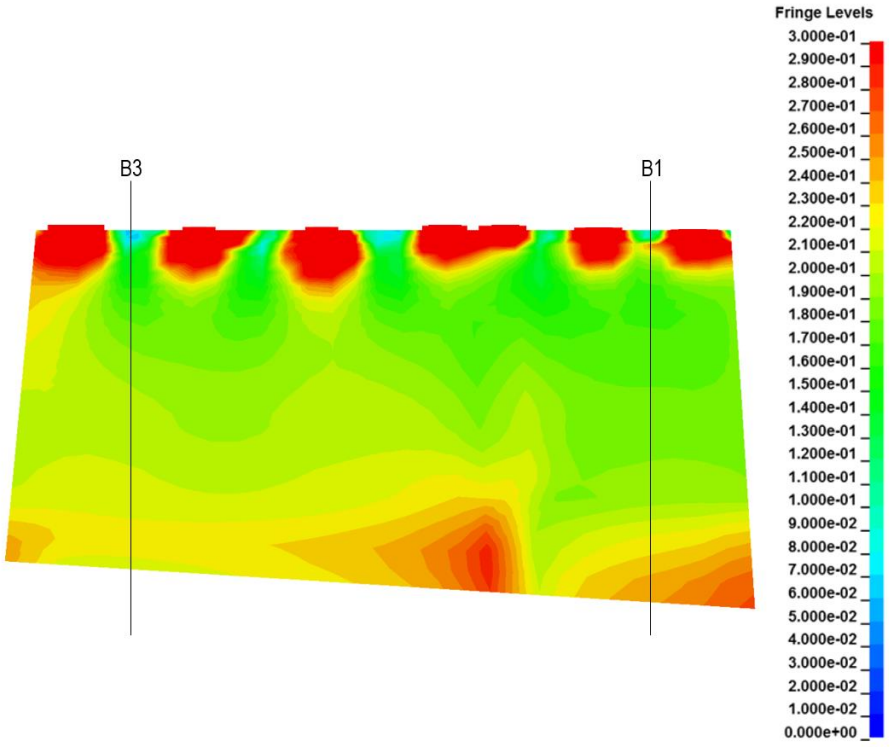

Figure 3.7: Contour plot of equivalent stress for 30% additional structural load. Cross-section through Pier 1 with marked boreholes B3 and B1.

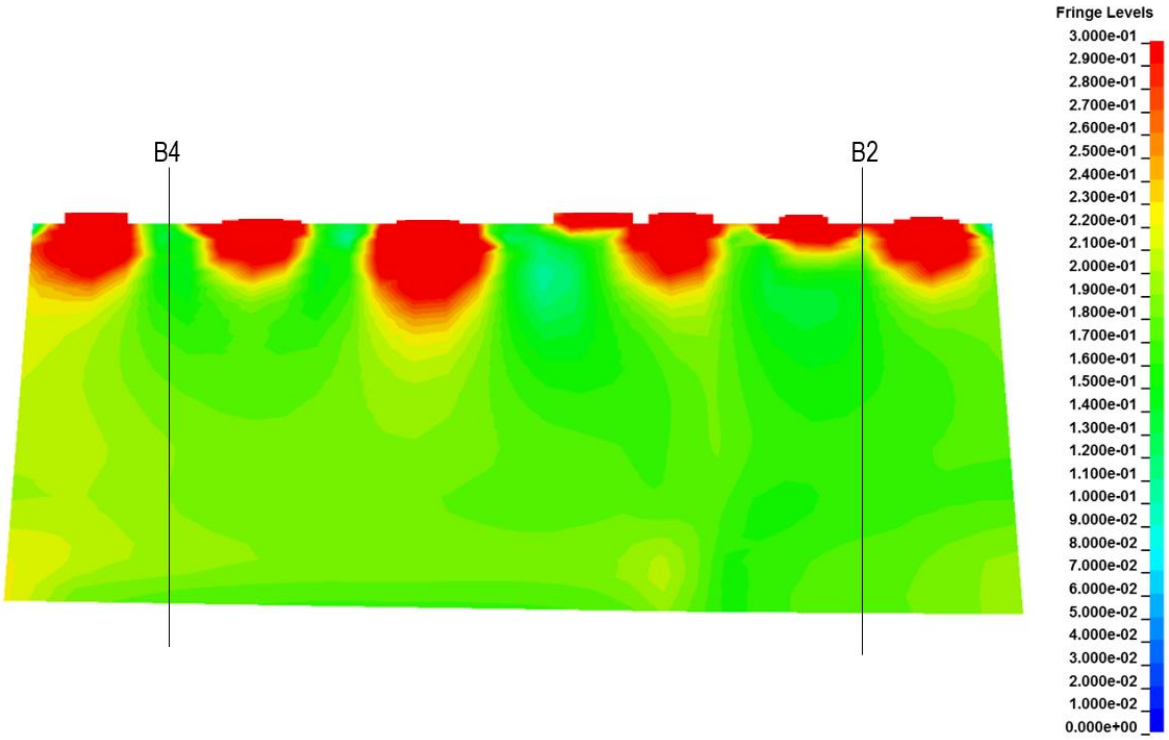

Figure 3.8: Contour plot of equivalent stress for 30% additional structural load. Cross-section through Pier 2 with marked boreholes B4 and B2.

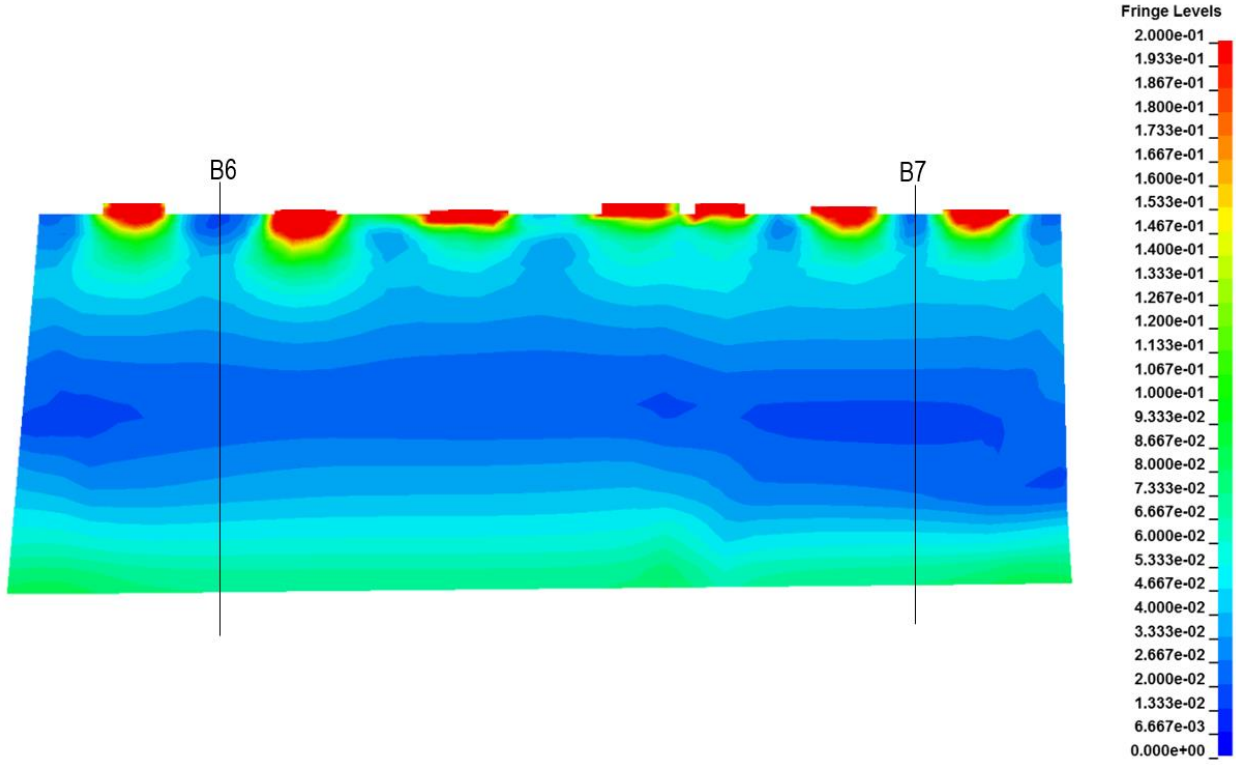

Figure 3.9: Contour plot of equivalent stress for 30% additional structural load. Cross-section through Abutment 2 with marked boreholes B6 and B7.

3.2. Static vehicular load

The second load case covers the live load acting on the structure. The American Association of State Highway and Transportation Officials (AASHTO) has a set of specifications for truck loadings to account for live load on bridges [6]. Live load due to traffic of vehicles for short-span bridges includes a standard HS20-44 three-axle truck load and a lane load, which are shown in Figure 3.10. The HS trucks are a representation of the actual loading caused by trucks and are the lowest design loads to ensure the minimum load carrying capacity of a bridge. The HS20-44 load is represented by three concentrated forces with a distance between them equal to 14 ft (4.27 m). Two of them are equal to 32,000 lbs (142 kN) and one equal to 8,000 lbs (35 kN). The lane load is a simplification of a 20-tonne truck preceded and followed by 15-tonne trucks and is a uniformly distributed load of $0.64\frac{kips}{ft}\left(9.34\frac{kN}{m}\right)$. It is assumed to occupy 10ft (3.05 m) in the transversal direction of the road. For 20-30 ft (6.10-9.14 m) curb-to-curb width of the bridge, two traffic lanes are to be used according to the specifications. This gives a distributed surface load of $\frac{0.64\frac{kips}{ft}}{15ft} = 0.043\frac{kip}{ft^2}$ (2.04 kPa) acting on the bridge model.

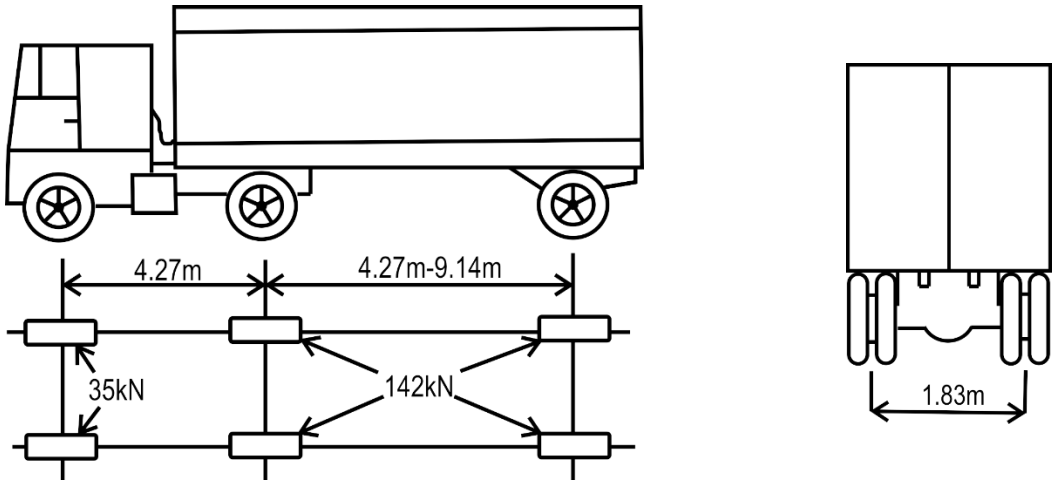

Figure 3.10: Basic design live load – truck load

All steel bridge girders have the same static diagram, shown in Figure 3.11. We are interested in the response of foundations, therefore we want to find positions of the truck load that give the highest stresses in the supports. The influence lines of reaction forces were drawn for Abutment 2 (RA) and Pier 2 (RB). Influence lines of reactions in the other two supports were not drawn due to the symmetry of the system. The least favorable position of the HS20-44 load was chosen and is presented in Figure 3.11.

In a three-dimensional case the truck is represented by six concentrated loads, four of them equal to 142 kN and two are 35 kN. Loads are applied over the girders and in-between them. This choice is made to find a position of the load which gives the highest stresses in the foundations. Cross-sections through the deck with two locations of the HS20-44 truck load are

depicted in Figure 3.12. In the first case the concentrated loads act in between the girders and in the second the forces are applied right above the girders.

Finally, four critical positions of the load were considered. Two for the abutment (RA position 1 and RA position 2) and two for the pier (RB position 1 and RB position 2), as shown in Figure 3.13. The results for four load cases, due to application of design live load, are shown. The design load consists of the lane load, which is distributed uniformly on the deck surface and the standard HS20-44 truck load. The truck load locations were chosen such that the reactions in the foundations are the highest.

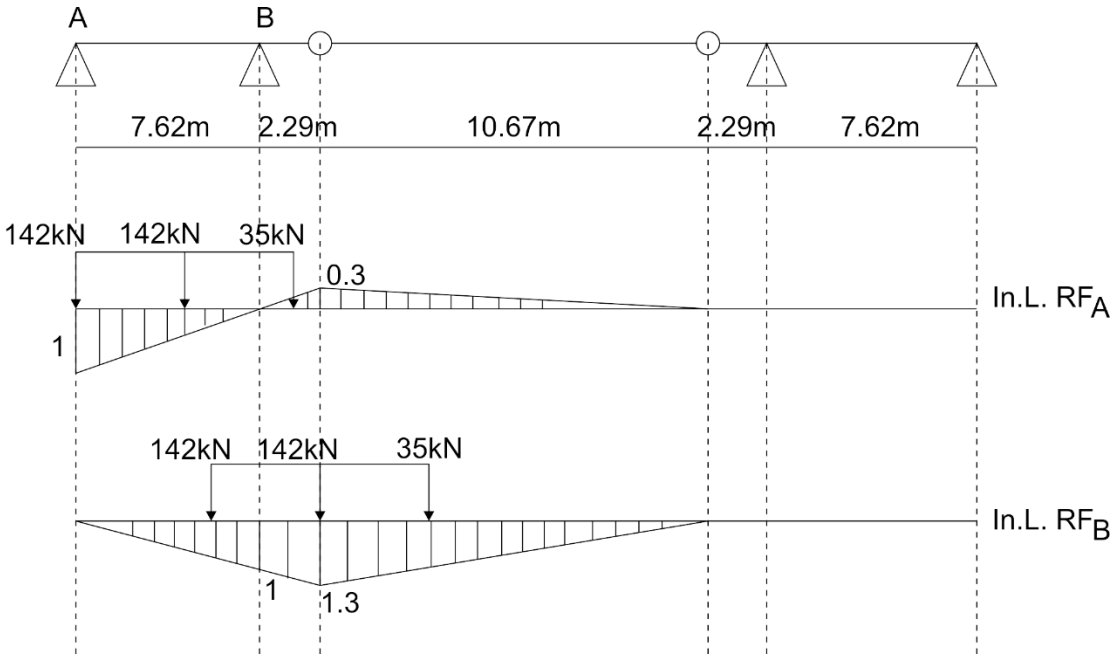

Figure 3.11: Static diagram of a representative girder. Influence lines of the reaction forces in Abutment 2 and Pier 2

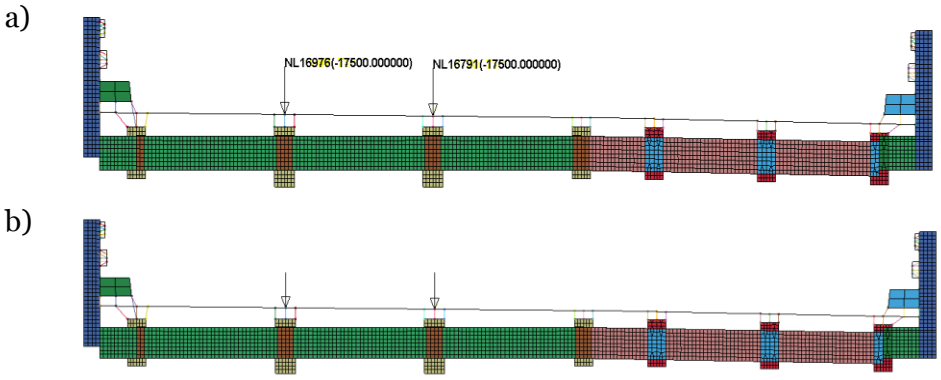

Figure 3.12: Cross-section through the deck with locations of the HS20-44 truck load with respect to the girders, (a) position 1, (b) position 2

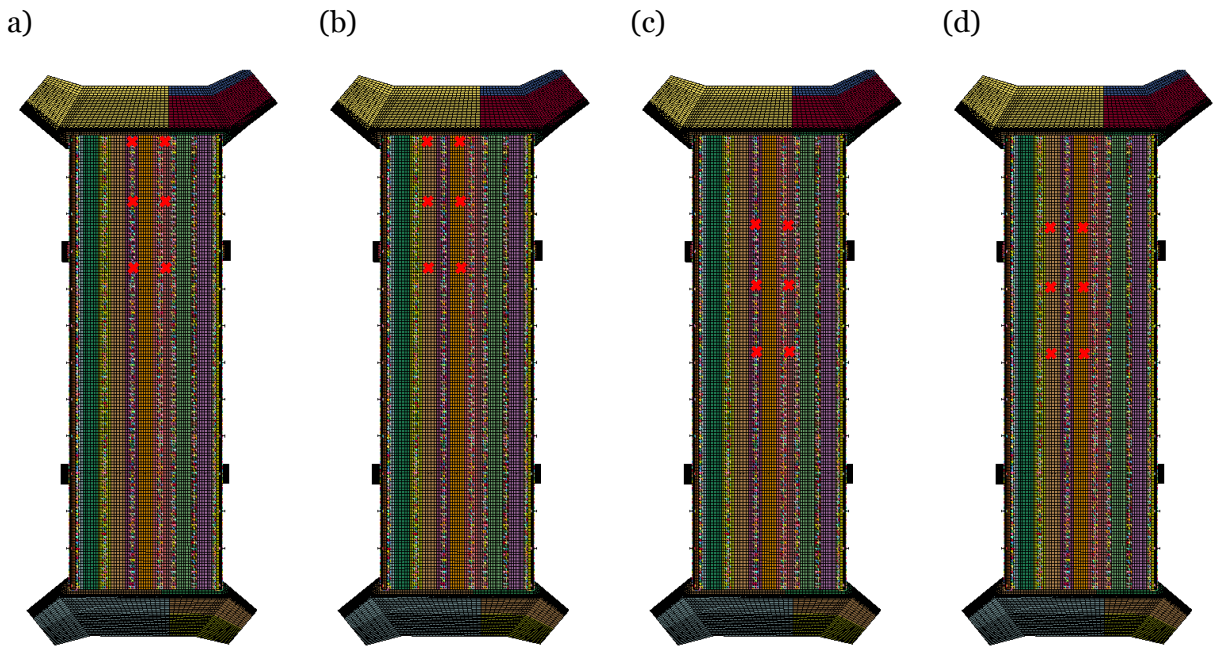

Figure 3.13: Critical positions of the standard truck load on the deck (a) RA position 1, (b) RA position 2, (c) RB position 1, (d) RB position 2. The forces are marked in red.

Maximum deflections in the middle span of the deck for the four load cases are compared to a base case, when only existing structural load is applied. Figure 3.14 shows deflections in six points on the deck under design live load, compared to the base case with only gravitational load of the structure. In each case the deflections have higher values than the base case, up to 7.8 mm in the worst scenario. In load cases RBpos1 and RBpos2, when the load is applied in a way that causes the highest stresses in Pier 2, the previously almost constant deflection changes and forms a deflection bowl. This occurs because the load is located closer to the output points.

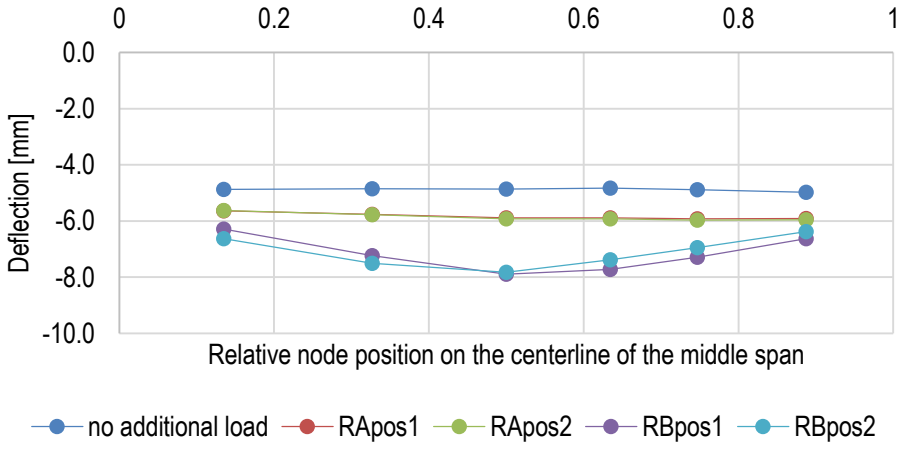

Figure 3.14: Deflections in six points on the deck under design live load. Locations of the static truck load, RApos1, RApos2, RBpos1 and RBpos2 are shown in Figure 3.13

The displacements on the foundations change in a non-uniform way due to different positions of the load. In every case the values are low, compared to the superstructure deflections, and don't exceed 0.01 mm for the abutments and 0.04 mm for the piers. Figure 3.15 presents vertical displacements of a chosen set of points on the substructure due to design live load.

a)

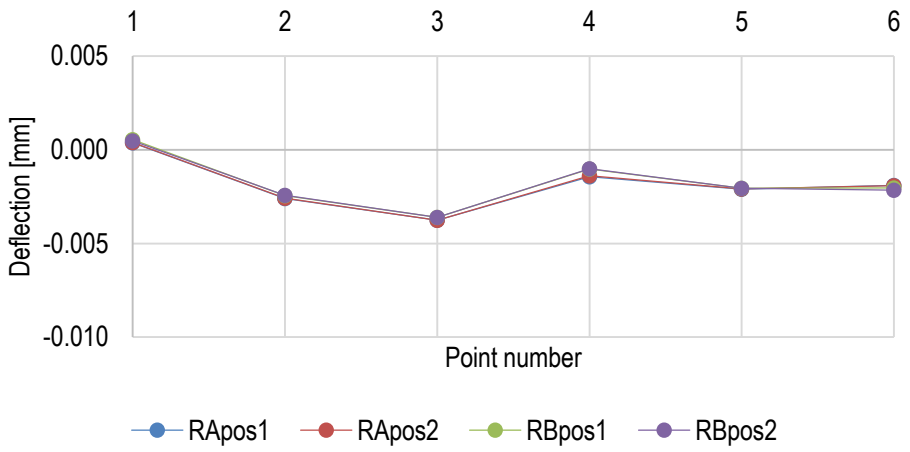

b)

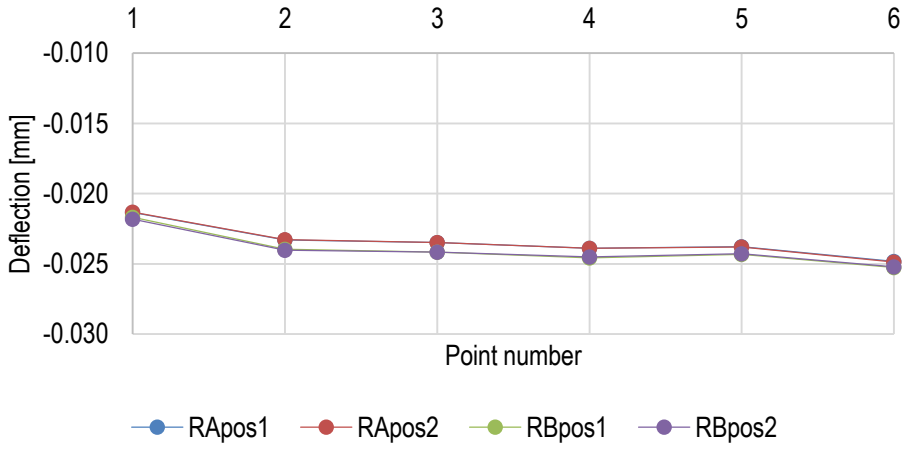

c)

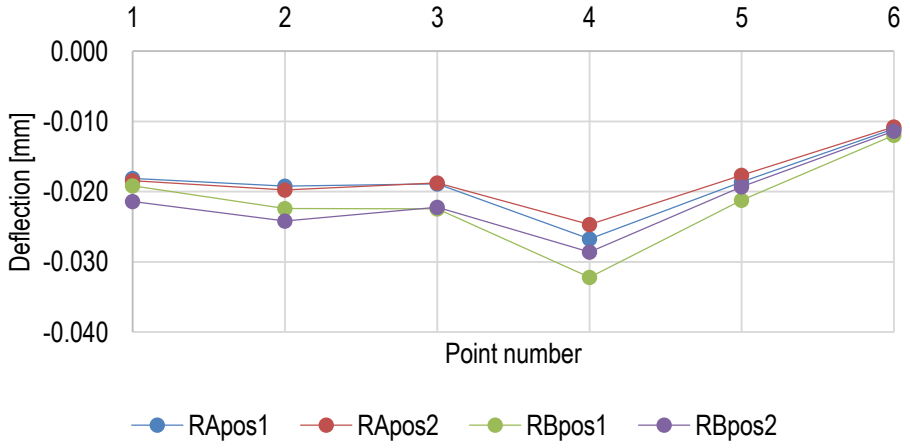

d)

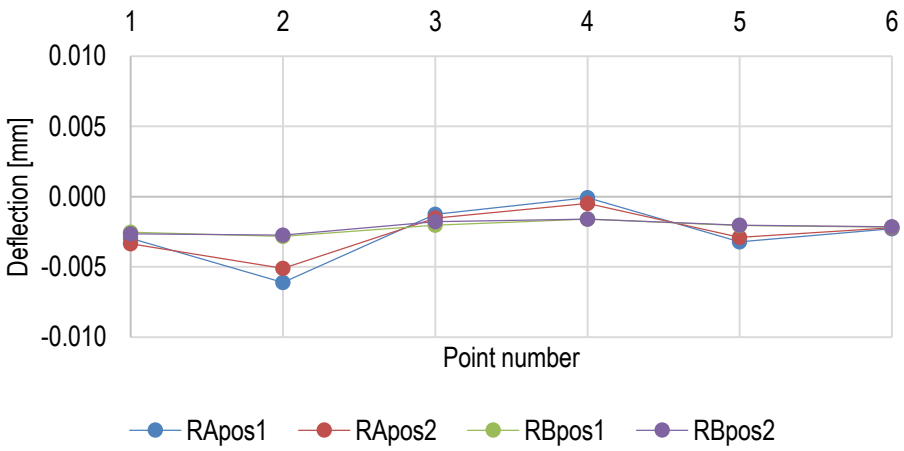

Figure 3.15: Vertical displacements of a chosen set of points on the substructure due to design live load; a) Abutment 1, b) Pier 1, c) Pier 2, d) Abutment 2. Locations of the static truck load, RApos1, RApos2, RBpos1 and RBpos2 are shown in Figure 3.13.

Table 3: Maximum values of von Mises stress in the foundations due to design live load

Load case	**no additional load**	**RApos1**	**RApos2**	**RBpos1**	**RBpos2**
Mises stress [MPa]	0.528	0.572	0.578	0.67	0.665
Percentage of used structural capacity	4.0%	4.3%	4.4%	5.1%	5.0%
Percentage of used geotechnical capacity	2.0%	2.2%	2.2%	2.5%	2.5%

In the case of static load due to critical position of a standard truck, maximum von Mises stress does not exceed a few percent of structural capacity of the foundations. The values obtained are shown in Table 3. Stress concentrations under the bearings of Pier 2 are more prominent in cases RBpos1 and RBpos2. The highest value of von Mises stress on the east wall of Pier 2 for case RBpo2 is seen under the central girder as seen on Figure 3.16, because it carries the highest loads: the truck load is located right over it and the deck is the thickest in this region.

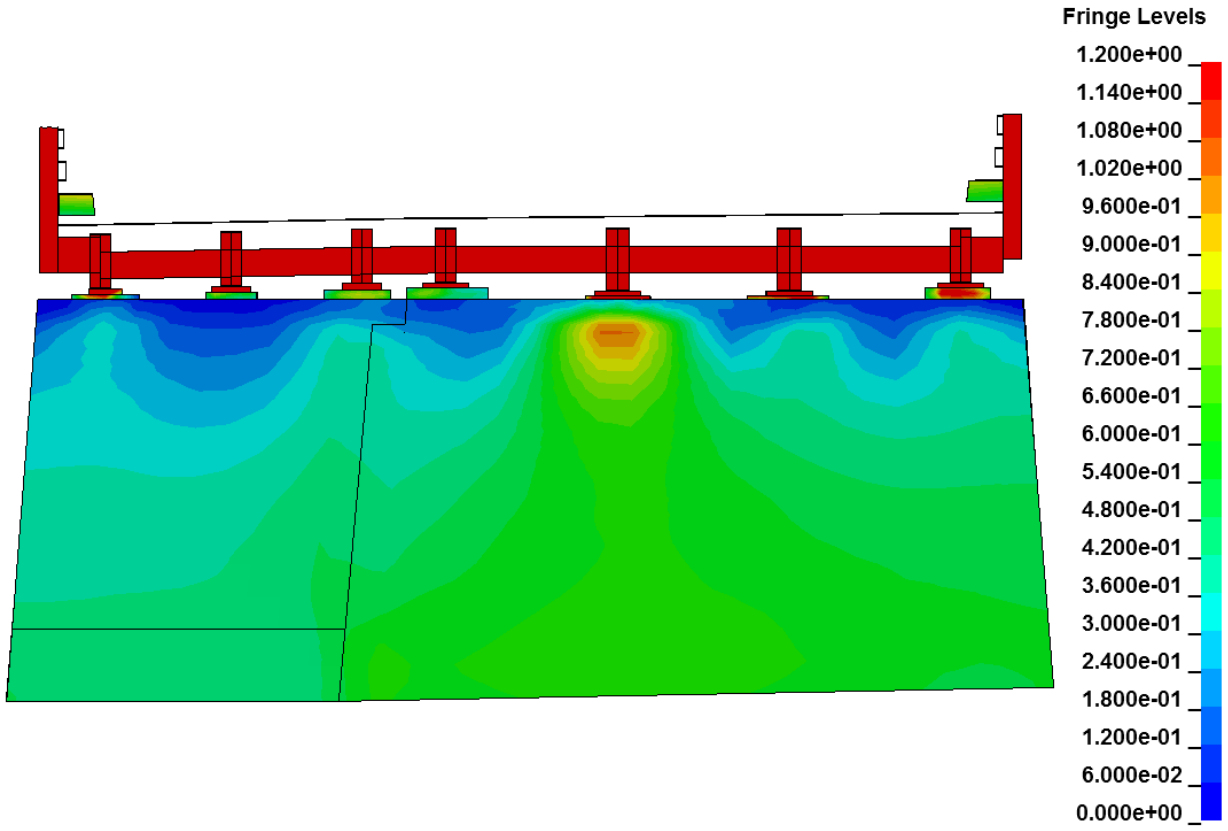

Figure 3.16: Von Mises stress on the east wall of Pier 2 for case RBpo2 (load location RBpos2 is shown in Figure 3.13).

According to the presented computational model, none of the considered static loads can cause a failure of the structure. Only a few percent of structural, as well as geotechnical, capacity are used. In this regard the foundations are safe for reuse with the assumption that no cracks present in the foundations will cause slip bands. The computational model doesn't include any cracks and the masonry is not modeled as a composite. Naturally, when the new design of the deck is known, additional calculations should be performed by structural engineers. The calculations should include the dead load of the new structure and construction loads, which can be of different nature than the ones described in this report.

3.3. Frequency analysis

An implicit eigenvalue analysis was performed to investigate the frequencies of the bridge. The default eigenvalue extraction method, which are Block Shift and Invert Lanczos, was chosen.

Table 4 presents the first 10 natural frequencies of the bridge calculated in LS-DYNA. The lowest natural frequency of 7.73 Hz is a bending mode and involves vertical vibrations of the deck. The second mode, at frequency 8.24Hz, is torsional. The 3rd to 7th modes describe bending vibrations of the structural elements of the bridge, whereas the 8th to 10th modes involve vibrations of the railings. Most of the bending modes result in vertical displacements of the deck, except for the fourth mode, which gives bending in the deck plane. Figure 3.17 to Figure 3.26 depict the resultant displacement contours in the first ten vibration modes. The values of resultant displacement normalized to range from 0 (dark blue) to 1 (red). Top view of the structure, as well as side view are shown. In all cases the vibrations of the foundations are negligibly small comparing to the response of the superstructure. Only in mode 5, presented on Figure 3.21, slight differences in color can be noticed.

Table 4: Natural frequency values and mode types

Mode nr	**1**	**2**	**3**	**4**	**5**	**6**	7	**8**	**9**	**10**
Frequency [Hz]	7.73	8.24	10.97	14.29	16.33	16.55	17.58	18.52	18.58	18.73
Mode type	B	T	B	B	B	B	B	NS	NS	NS

B-bending, T-torsional, NS-nonstructural

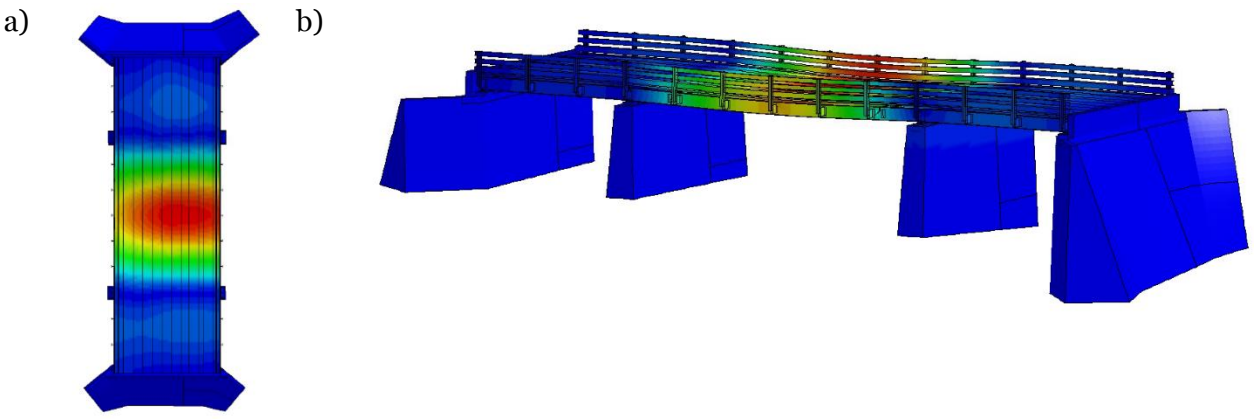

Figure 3.17: First vibration mode - contours of resultant displacement a) top and b) side view

a) b)

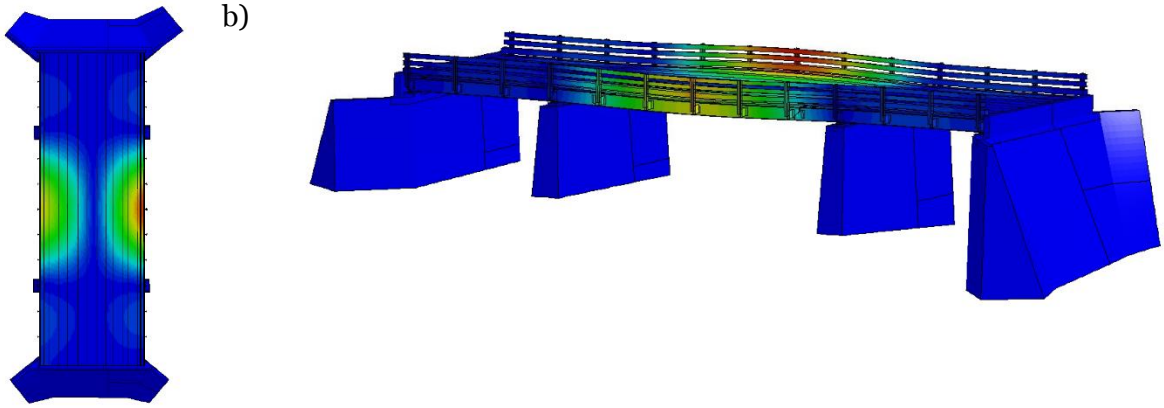

Figure 3.18: Second vibration mode - contours of resultant displacement a) top and b) side view

a) b)

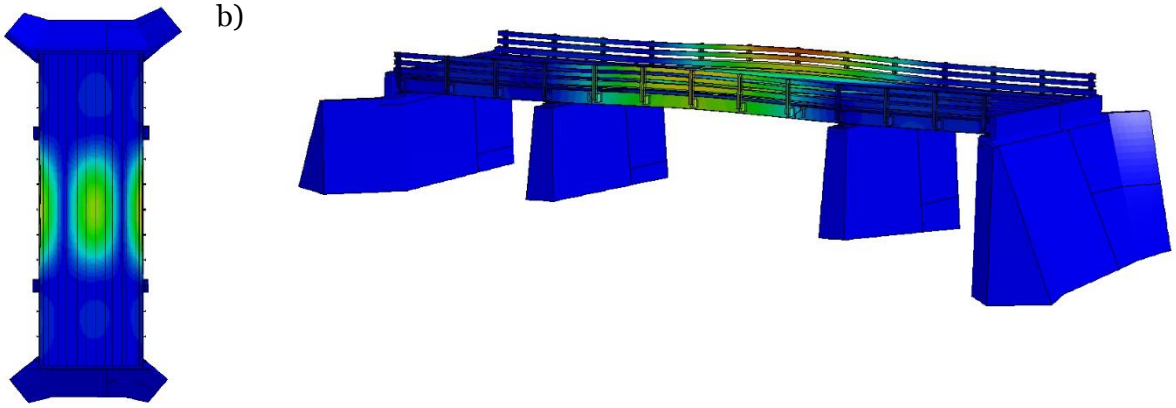

Figure 3.19: Third vibration mode - contours of resultant displacement a) top and b) side view

a) b)

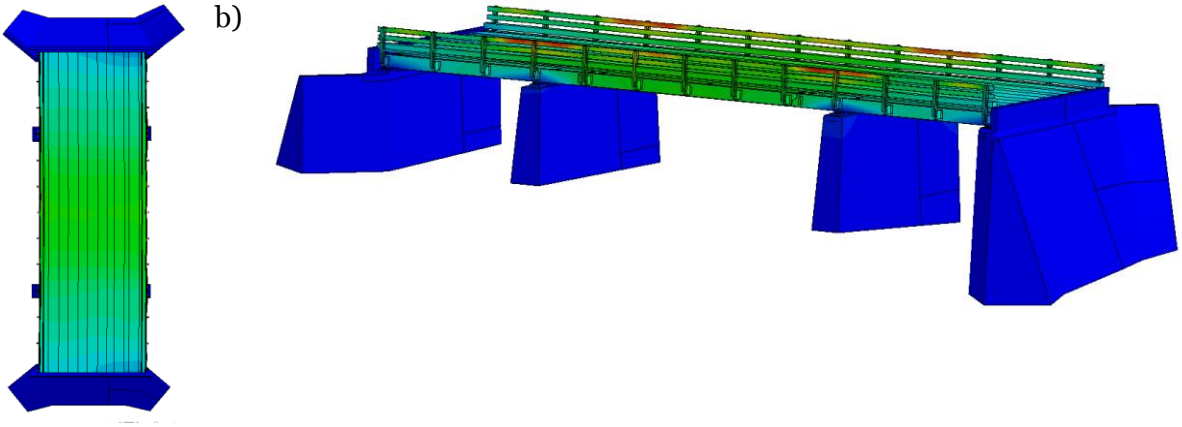

Figure 3.20: Fourth vibration mode - contours of resultant displacement a) top and b) side view

a) b)

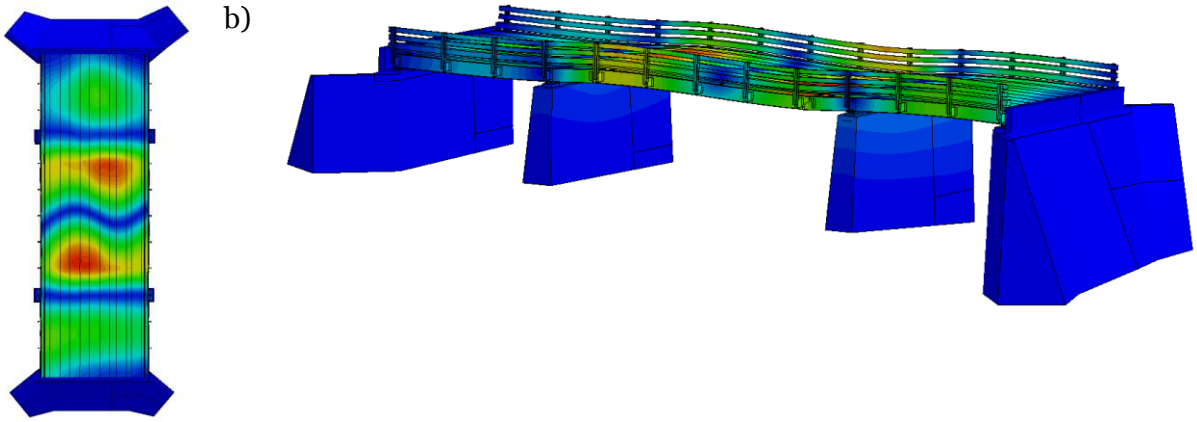

Figure 3.21: Fifth vibration mode - contours of resultant displacement a) top and b) side view

a) b)

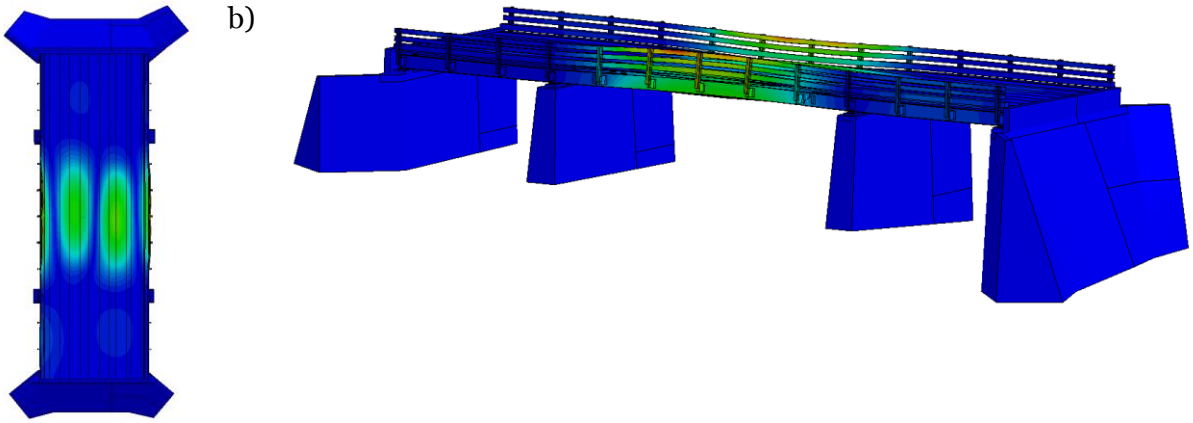

Figure 3.22: Sixth vibration mode - contours of resultant displacement a) top and b) side view

a) b)

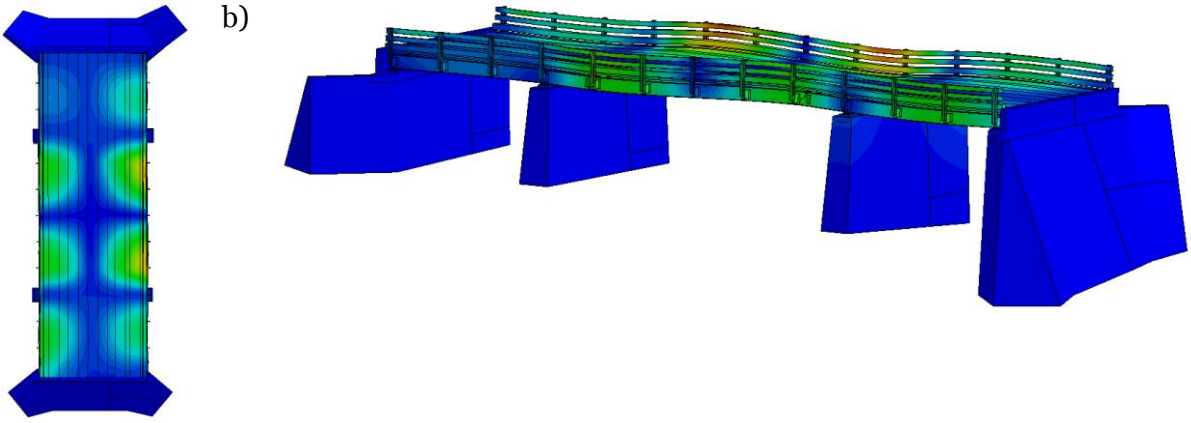

Figure 3.23: Seventh vibration mode - contours of resultant displacement a) top and b) side view

a) b)

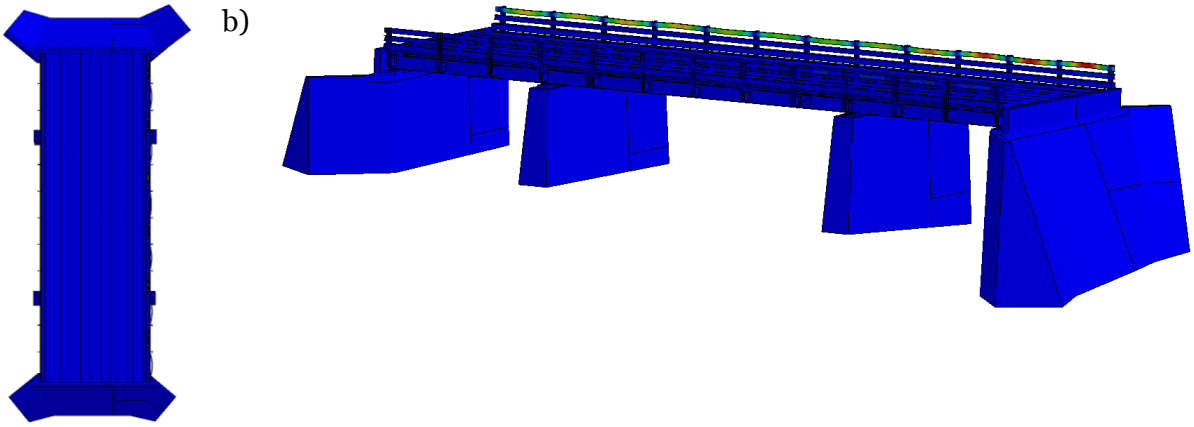

Figure 3.24: Eighth vibration mode - contours of resultant displacement a) top and b) side view

a) b)

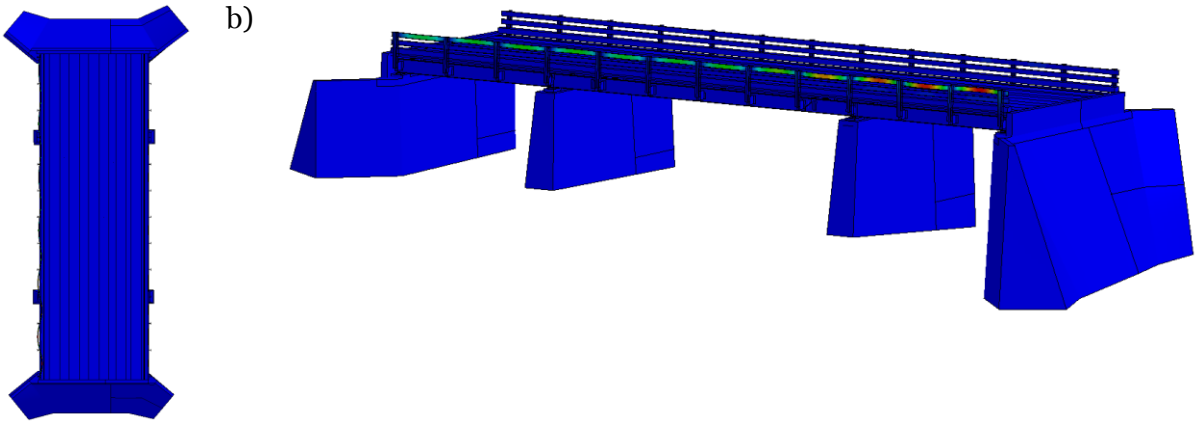

Figure 3.25: Ninth vibration mode - contours of resultant displacement a) top and b) side view

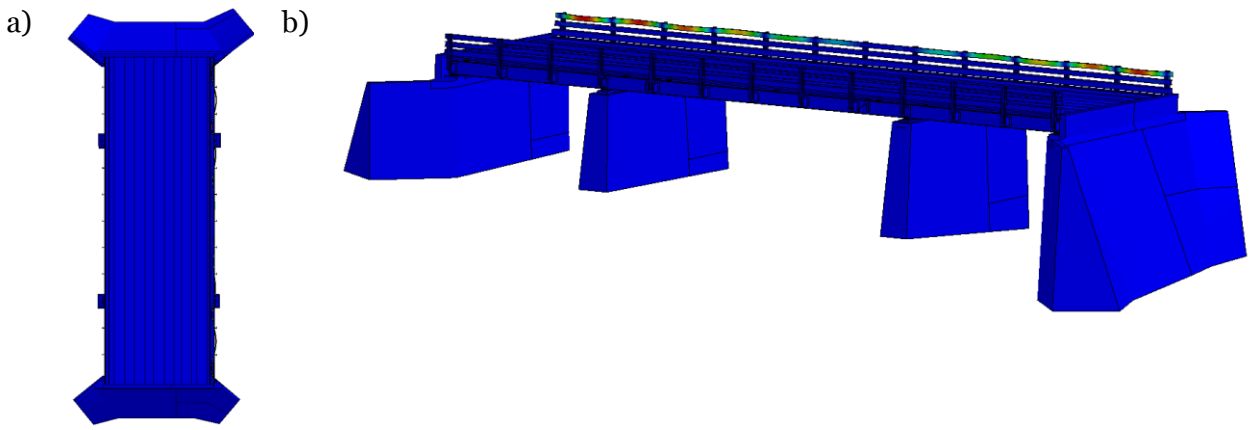

Figure 3.26: Tenth vibration mode - contours of resultant displacement a) top and b) side view

3.4. Dynamic vehicular load

Dynamic loading of the bridge due to vehicular traffic was considered. A finite element model of a tractor-trailer truck developed as part of research conducted at Florida State University, Tallahassee, FL [7] was used to analyze the response of the structure. The vehicle model represents a Mack CH613 truck tractor with a three axle single drop lowboy trailer, of total mass of 53 tons (117,000 lbs). A photograph of the truck and its finite element model are shown in Figure 3.27. It is the heaviest vehicle tested in the mentioned study. Additional cargo was distributed evenly on the deck in the form of four loads: Load_1 – 2.75 tons, Load_2 – 4 tons, Load_3 – 13.88 tons, Load_4 – 9.2 tons.

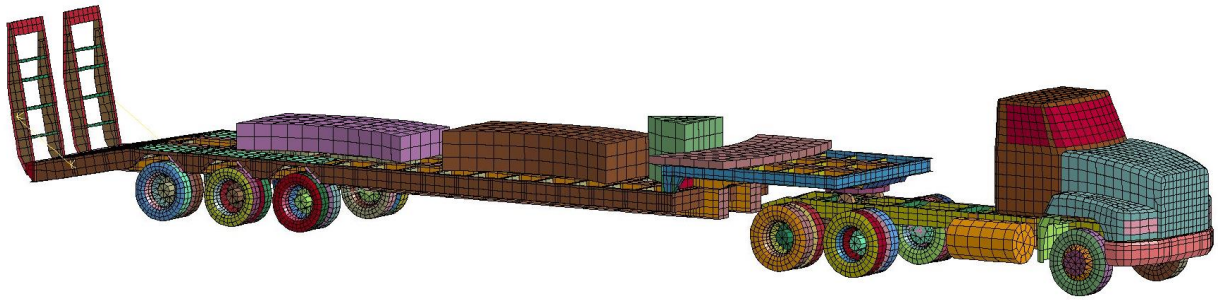

Figure 3.27: Mack CH613 truck tractor and its finite element model

In order to join the two models, the model of the bridge with the model of the truck, an approach slab had to be added. The approach consists of two parts. First one, further away from the bridge deck, is modeled with rigid solid finite elements. Second, the main part, is built of deformable solid finite elements with properties of concrete (defined as an elastic material model). Moreover, a section of rigid wall was added before the approach and on the other end of the bridge to allow for a correct movement of the truck along the bridge. The section that connects the approach with the slab had to be located on the appropriate height, so that there is a smooth transition between surfaces and no unwanted additional vibrations are present. The interaction

between the truck wheels and deck surface is achieved by defining a surface-to-surface contact with static and dynamic coefficients of friction equal to 0.65.

Five runs of the truck traveling with a speed of 55 mph, which is the limit speed on this road, are considered. They differ with the position of the truck on the transversal cross-section of the bridge. These are presented on Figure 3.28.

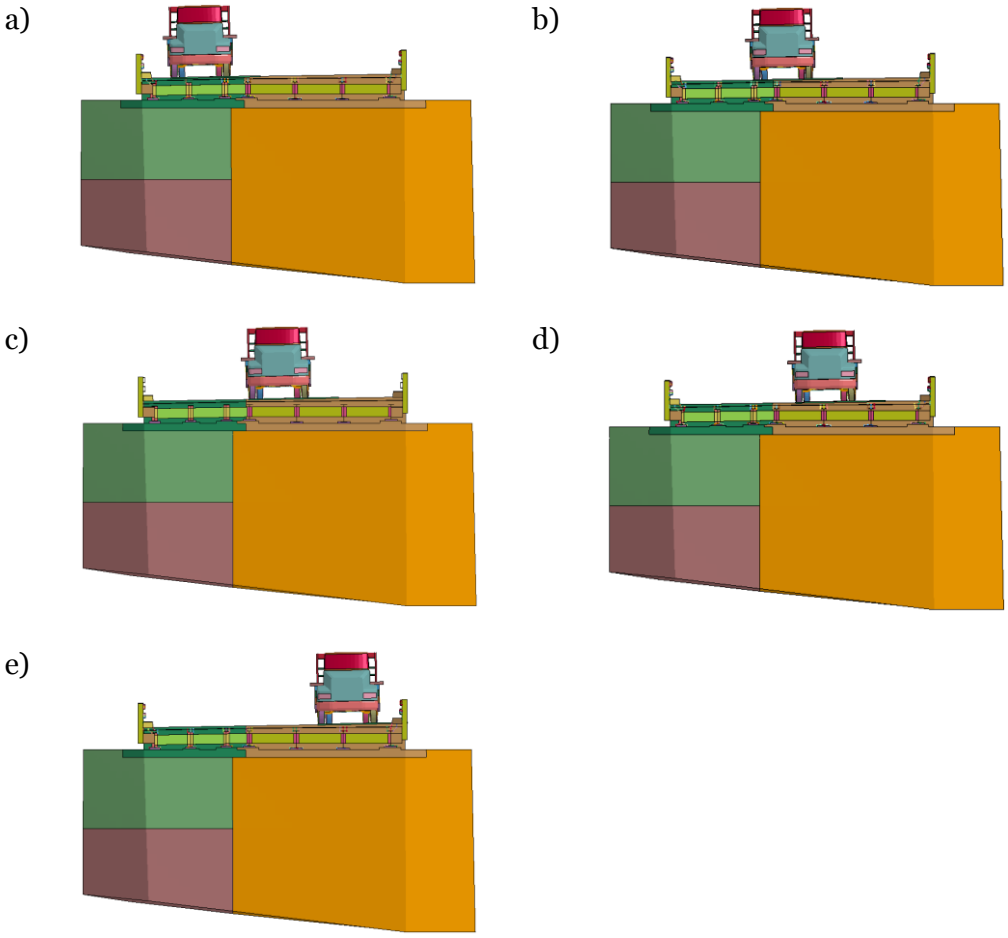

Figure 3.28: The considered positions of the truck on the bridge: a) position 1, b) position 2, c) position 3, d) position 4, e) position 5

Figure 3.29 shows the dynamic response of the structure caused by a truck moving along the road. At the beginning of the computations the truck is located outside of the bridge. It enters the bridge at time t=2.2 s and leaves it at time t=4.1 s.

The vertical displacements of the deck and foundations were recorded in the same locations as for the static load case. They are presented in Figure 3.3. This way it is possible to make a quantitative comparison between static and dynamic behavior of the bridge. The greatest increase of the deck deflections is noted in the first load case (which is position 1 shown on Figure 3.28), when the truck runs close to south-side curb. Maximum deflection is recorded between first

two girders and equals 10.3 mm (at time t=3.4s), which is twice as much as in static case. Figure 3.29presents time-deflection curves for nodes on the deck for position 1 of the truck.

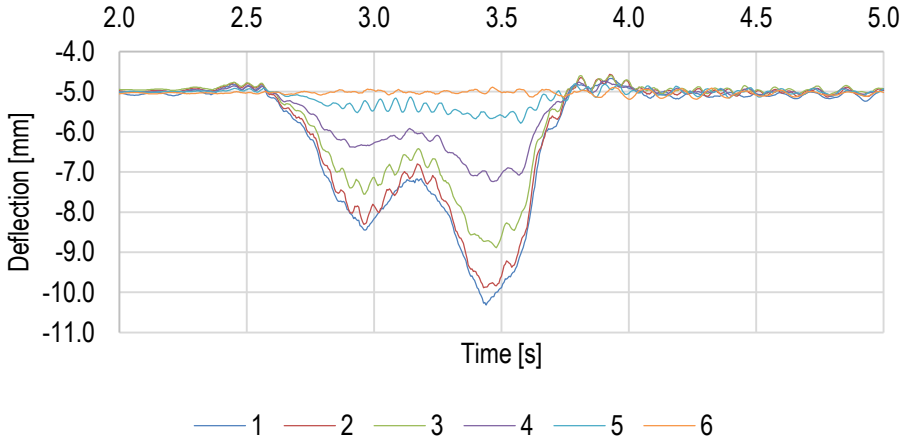

Figure 3.29: Time-deflection curves for nodes on the deck for position 1 of the truck. Locations of points 1- 6 are shown on Figure 3.2.

The highest recorded vertical displacements of six nodes on the deck are shown in Figure 3.30. They are compared with the base case, with structural load only. Qualitative differences in the deflection curves are apparent with regards to the position of the load. The same trend are seen on the graphs which show vertical displacements of points on top surfaces of foundations. Vertical displacements of a chosen set of points on the foundations due to dynamic truck load are depicted in Figure 3.31.

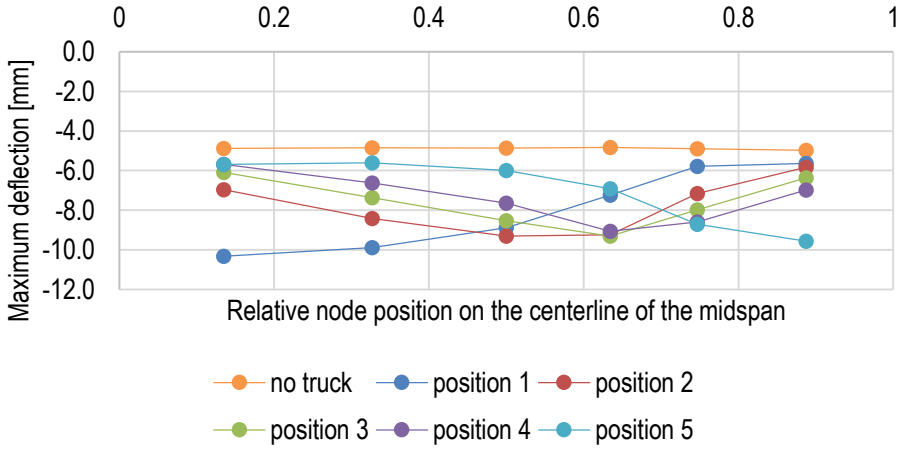

Figure 3.30: Maximum vertical displacements of nodes on the deck

a)

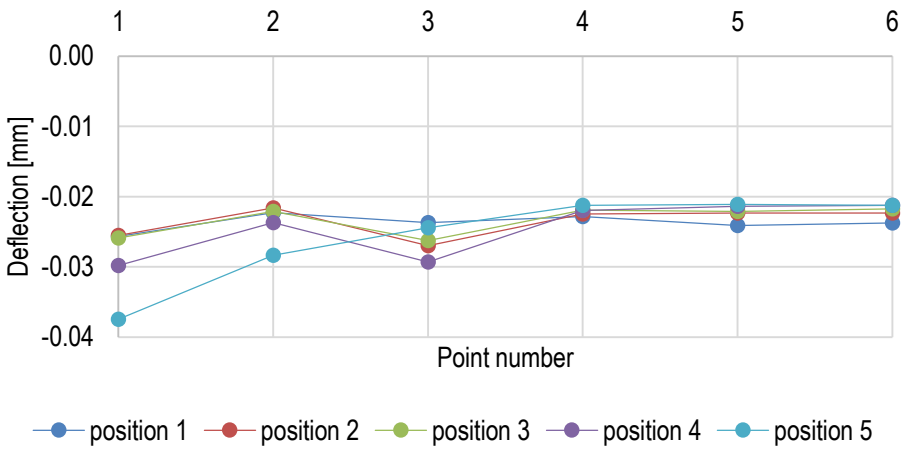
1
2
3
4
5
6
0.00
-0.01
-0.02
-0.03
-0.04
Deflection [mm]
Point number
position 1
position 2
position 3
position 4
position 5

b)

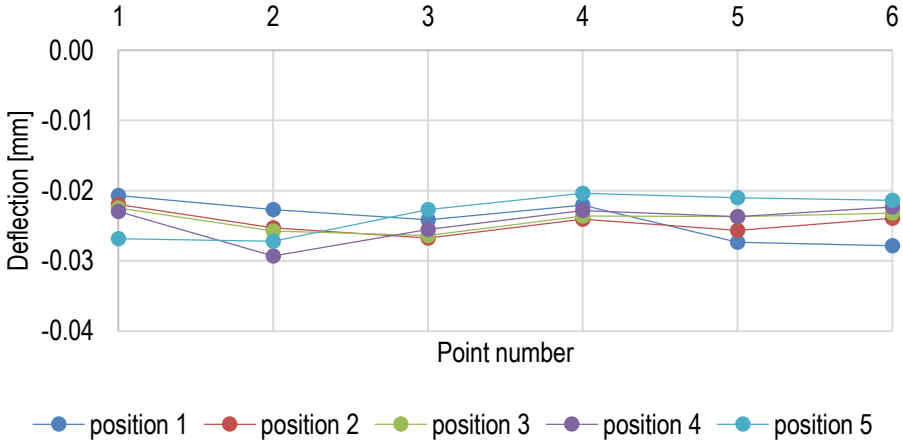
1
2
3
4
5
6
0.00
-0.01
-0.02
-0.03
-0.04
Deflection [mm]
Point number
position 1
position 2
position 3
position 4
position 5

c)

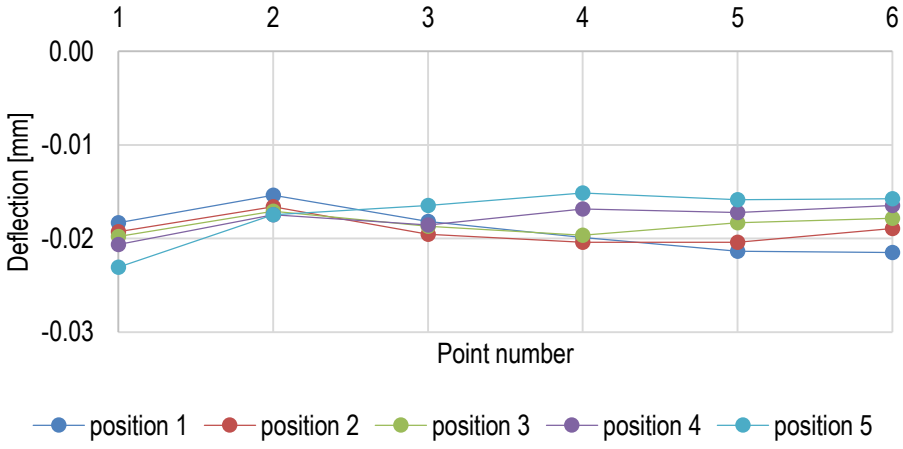
1
2
3
4
5
6
0.00
-0.01
-0.02
-0.03
Deflection [mm]
Point number
position 1
position 2
position 3
position 4
position 5

d)

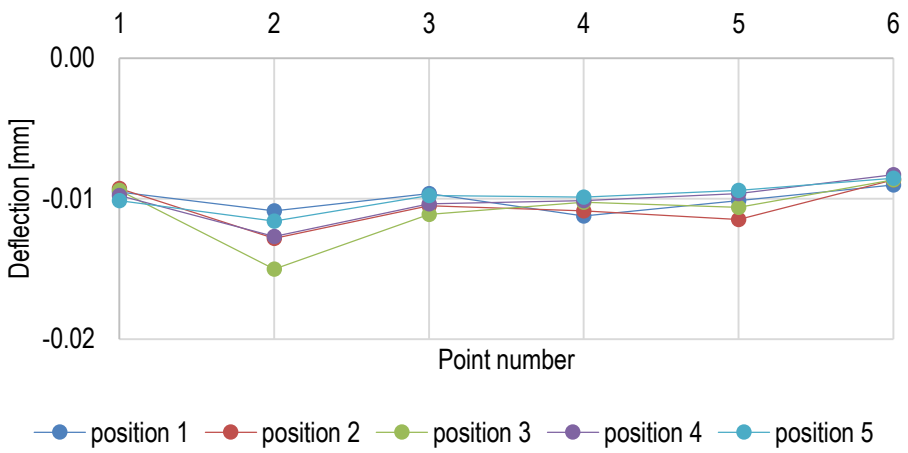

Figure 3.31: Vertical displacements of a chosen set of points on the foundations due to dynamic truck load a) Abutment 1, b) Pier 1, c) Pier 2, d) Abutment 2

The equivalent stress reaches the highest values at the bottom of Pier 1, in the old part of the foundation close to the joint plane with the new part. Figure 3.32 shows the maximum value of Mises stress at the bottom of Pier 1 measured at five different locations defined in Figure 3.3. The highest value of equivalent stress is reached at the bottom of Pier 1. Extreme values are recorded for loading case 1, as defined in Figure 3.28, and differ in time from 0.36 MPa to 0.75 MPa.

The evaluation of used percentage of structural and geotechnical capacity is shown in Table 5. The calculations are performed with the use of Equation 1.

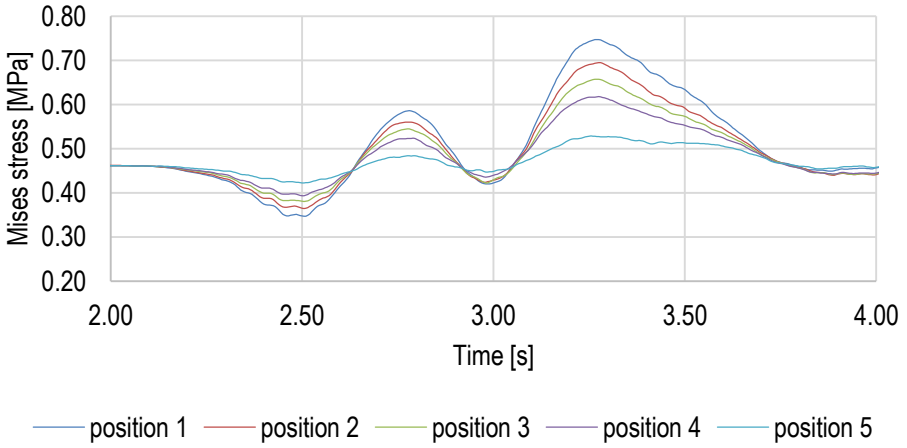

Figure 3.32: Maximum value of von Mises stress in function of time at the bottom of Pier 1

Table 5: Maximum values of von Mises stress in the foundations due to dynamic load

Load case	Position 1	Position 2	Position 3	Position 4	Position 5
Mises stress [MPa]	0.75	0.70	0.66	0.62	0.53
Percentage of used structural capacity	5.7%	5.3%	5.0%	4.7%	4.0%
Percentage of used geotechnical capacity	2.8%	2.6%	2.5%	2.3%	2.0%

3.5. Impact load

Modal testing (structural frequency response testing) is a form of vibration testing with the objective to find natural frequencies of a structure. The chosen set of tests is intended to allow examination of the influence of the maximum load value, the location of the impact point, and the presence of cracks on the structural response, meaning the accelerations in chosen nodes and first natural frequency.

Sledge hammer impact testing is considered as a reliable and inexpensive modal testing method. Usually it is used to evaluate small, lightweight or slender structures. In large civil engineering structures the signal-to-noise ratio decreases, which can cause problems with measurement data interpretation. Three values of impact load were considered. The first simulation represents modal sledge hammer testing. The heaviest hammer available, with the head weight of 12 lb (5.44 kg), was chosen. The impact force in this case is equal 44,400 N (10,000 lbf) [8].

A modified FWD method was also used in this study, which was developed as part of FHWA project [9]. It consists of applying dynamic impact loads at various points on the bridge deck, which approximate loads caused by truck wheels. The typical load range for FWD tests is 16,000-34,000 lbf (71-150 kN) and the typical pulse time range is 20-34 ms [10]. The maximum impact load was chosen equal to 133.5 kN. Another case two times smaller, P_{max}= 66.75 kN, was considered as well.

In each case the load function is defined as a triangular function with duration of 0.03 s with the maximum load P_{max}. It is shown in Figure 3.33.

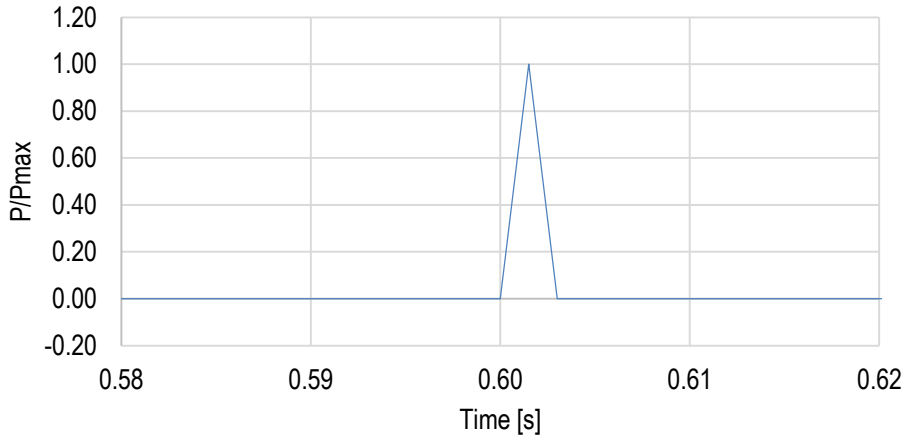

Figure 3.33: Impact load function defined in LS-DYNA

Four impact point locations were chosen. The input and output points are located on the top surfaces of both abutments and piers, supports' walls, as well as on the deck. Their distribution is presented in Figure 3.34.

Two boreholes drilled in Pier 2 and Abutment 2 showed that there vertical cracks, in the north-south direction, present in the old masonry section. Impact point loads are often used to establish existence of cracks and voids in structures if they're not visible from the outside. To verify this method, two modified models were developed. In the first one, one 2 mm-thick surface crack was added. In the next, a second, is a 5 mm-thick surface crack was added. Locations of the cracks introduced to the original model are presented on Figure 3.35. Cracks are modeled as gaps between finite elements (by detaching the finite elements and translating chosen nodes away from the second layer) with surface-to-surface contact, which eliminates the possibility of penetration of finite elements. The impact was applied in the input point 1, meaning on the top surface of Pier 2, in the SW part of the foundation.

a)

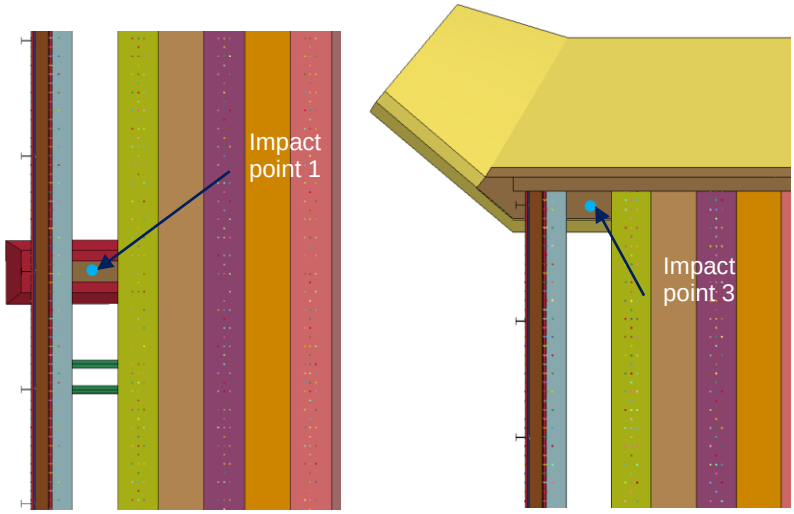

b)

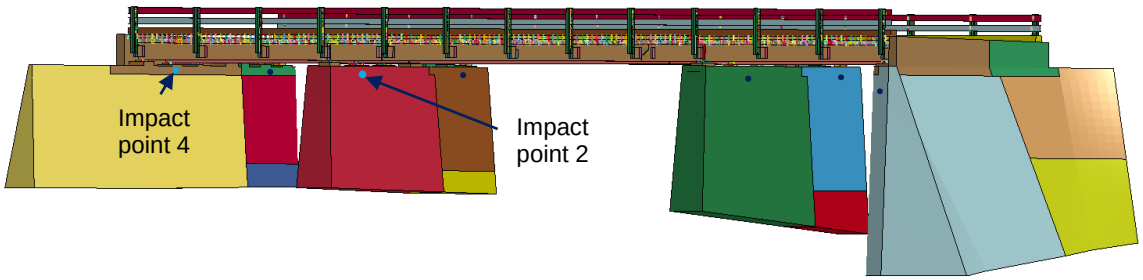

c)

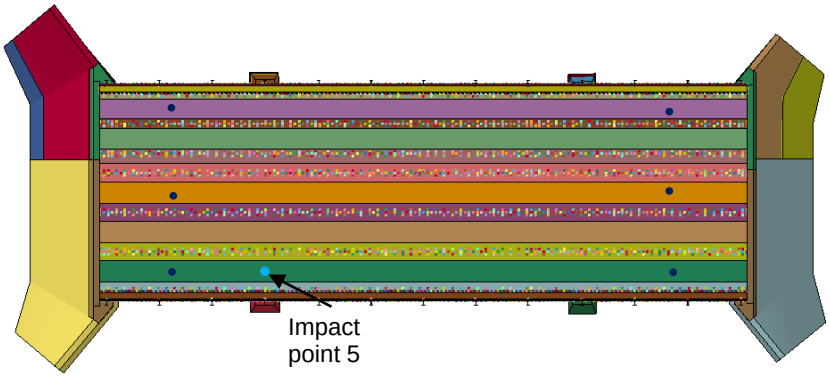

Figure 3.34: Input (marked in blue) and output (marked in black) points for the tests setups, on (a) top surfaces of the supports, (b) support walls, (c) the deck surface

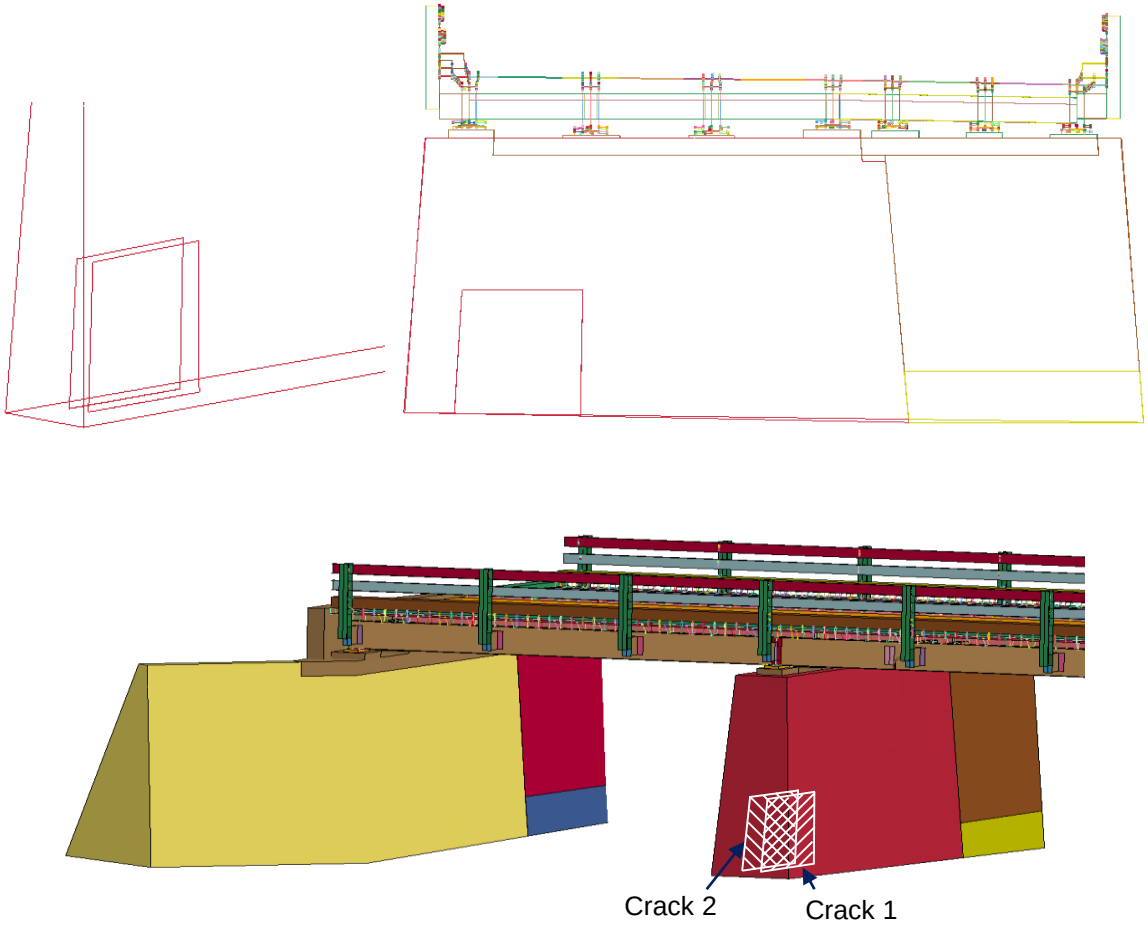

Figure 3.35: Locations of the cracks introduced to the original model

The test cases covered in this section examine the influence of the maximum value of the impact force P_{max}, location of the point of impact and presence of cracks, on the structural response. The chosen load cases are used to evaluate the possibility of applying this kind of test in structural integrity analysis.

3.5.1. Wave transfer in the structure

In this test the impact load is applied to the top (horizontal) surface of Pier 2 in the old section, between first and second girder. The maximum value of the load is P_{max}=133.5 kN. The accelerations of output points are presented separately for every point in Figure 3.36 to establish what differences can be seen from point to point.

Figure 3.36 (a) to (f) show graphs of the accelerations in the Y-direction (horizontal, along the roadway) as a function of time at output points on the substructure. The extreme value -12 m/s² was obtained at the point of impact (P2-2). The recordings at the output point (P2-3) on the same pier, but in the old section, give smaller acceleration values of 2 m/s². Moreover, the nonzero values appear with delay. That shows the influence of the structural damping. The

acceleration values for other output points decrease even more with the increasing distance from the impact. The lowest was received at a point furthest away from the impact, at Abutment 1 (Ab1-1), with extreme value of 0.004 m/s². Such small values may not be recorded by accelerometers during onsite tests. For that reason, it is recommended to perform many tests in various places on the structure, with a significant number of output points.

Accelerations were also recorded on several nodes on the deck. They are located on the back-spans of the bridge, across the roadway. Their exact locations are shown in Figure 3.35 (c). Vibrations in Z-direction were chosen for comparison, because they are most prominent in the superstructure (comparing to horizontal vibrations). Figure 3.37 shows separate graphs for each of the points. Values of the greatest acceleration are smaller (the highest about 2 m/s²) than in the foundations and the smallest are above 0.2 m/s² (which is a higher value than for the foundations).

a)

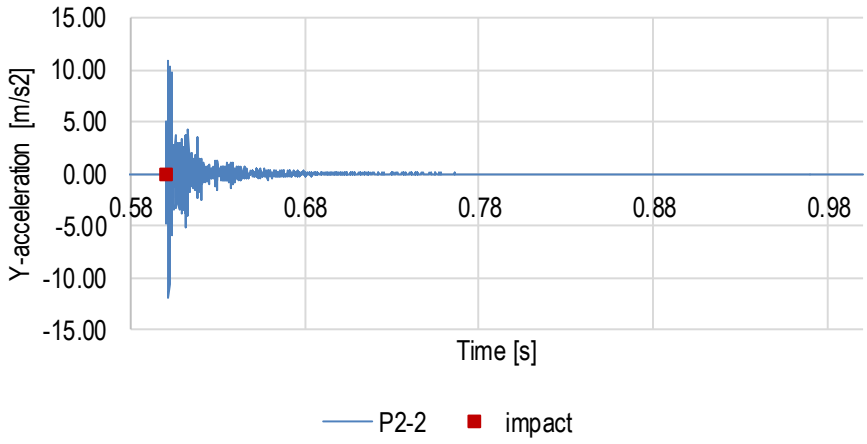

b)

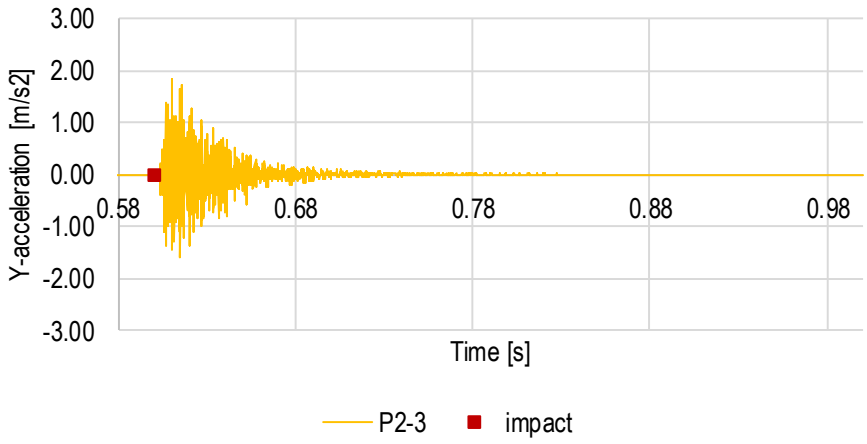

c)

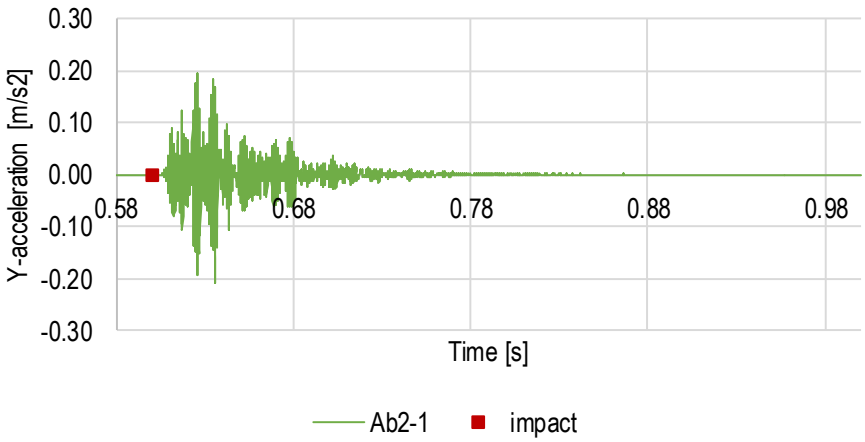
0.30
0.20
0.10
0.00
-0.10
-0.20
-0.30
Y-acceleration [m/s2]
0.58
0.68
0.78
0.88
0.98
Time [s]
Ab2-1
impact

d)

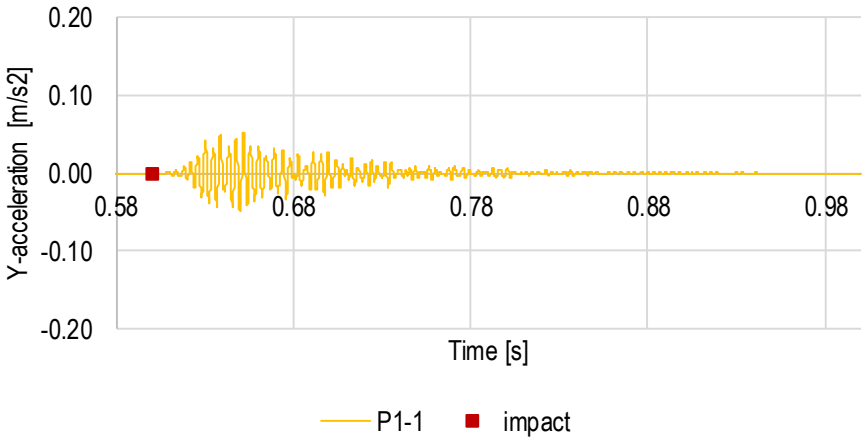
0.20
0.10
0.00
-0.10
-0.20
Y-acceleration [m/s2]
0.58
0.68
0.78
0.88
0.98
Time [s]
P1-1
impact

e)

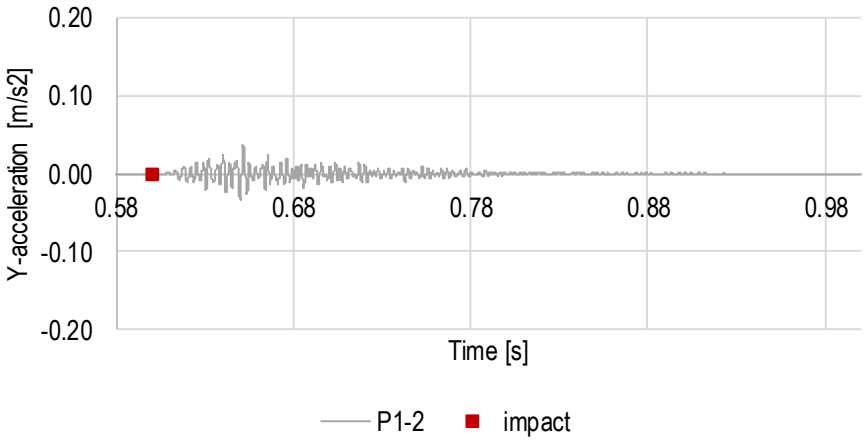
0.20
0.10
0.00
-0.10
-0.20
Y-acceleration [m/s2]
0.58
0.68
0.78
0.88
0.98
Time [s]
P1-2
impact

f)

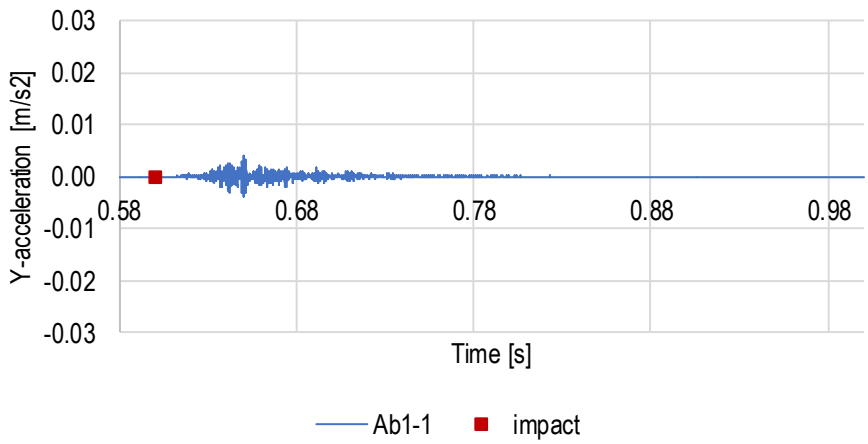

Figure 3.36: Y-acceleration vs. time curves of output nodes on the substructure. Time of impact is marked with a red square. Locations of the points are presented in Figure 3.34.

a)

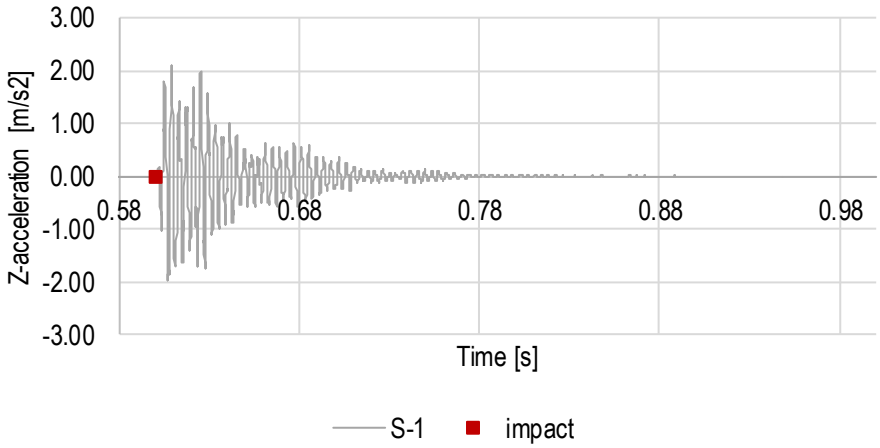

b)

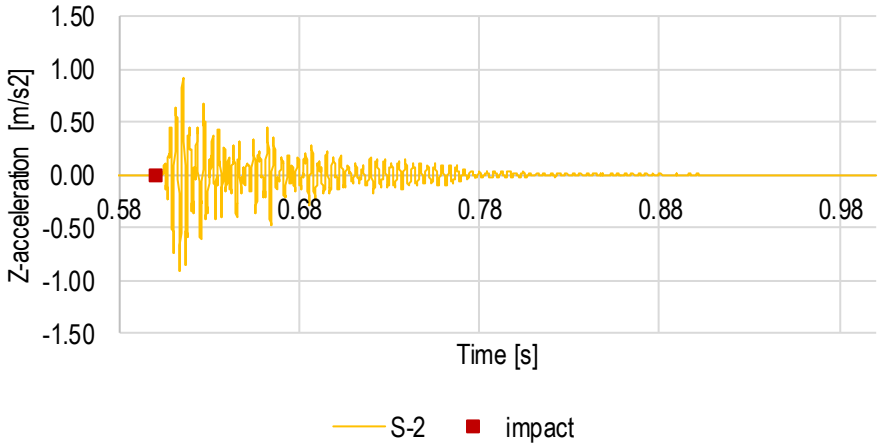

c)

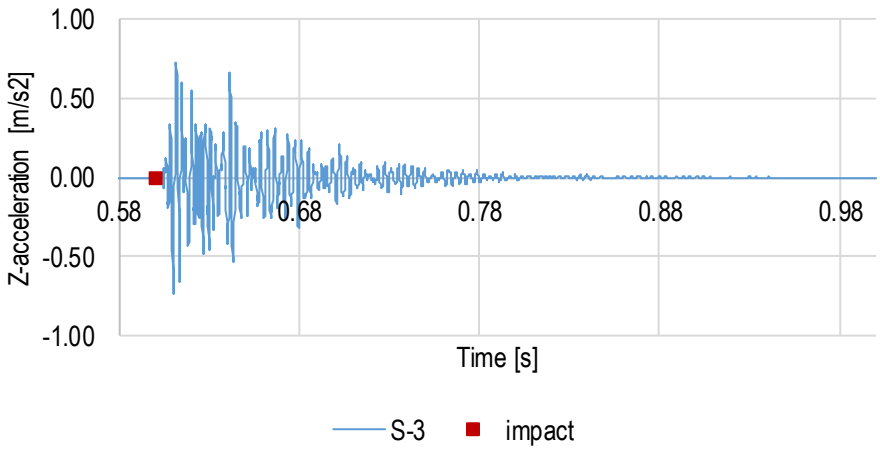
1.00
0.50
0.00
-0.50
-1.00
Z-acceleration [m/s2]
0.58
0.68
0.78
0.88
0.98
Time [s]
S-3
impact

d)

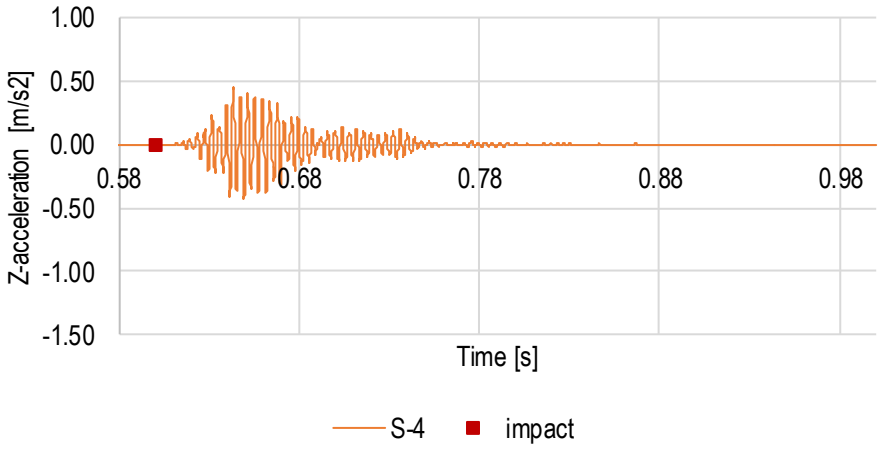
1.00
0.50
0.00
-0.50
-1.00
-1.50
Z-acceleration [m/s2]
0.58
0.68
0.78
0.88
0.98
Time [s]
S-4
impact

e)

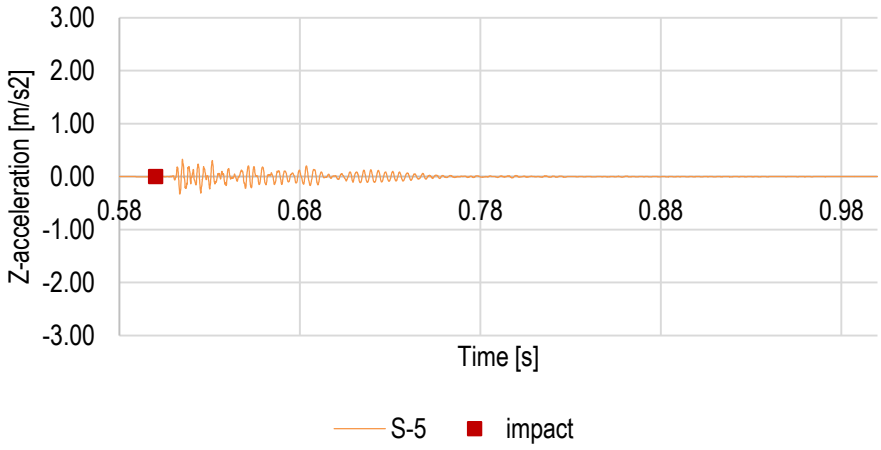
3.00
2.00
1.00
0.00
-1.00
-2.00
-3.00
Z-acceleration [m/s2]
0.58
0.68
0.78
0.88
0.98
Time [s]
S-5
impact

f)

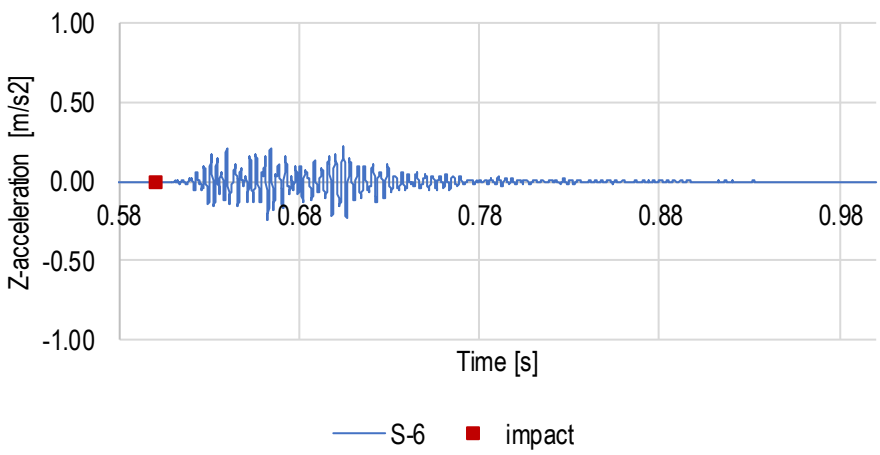

Figure 3.37: Vertical acceleration vs. time curves of output points on the superstructure

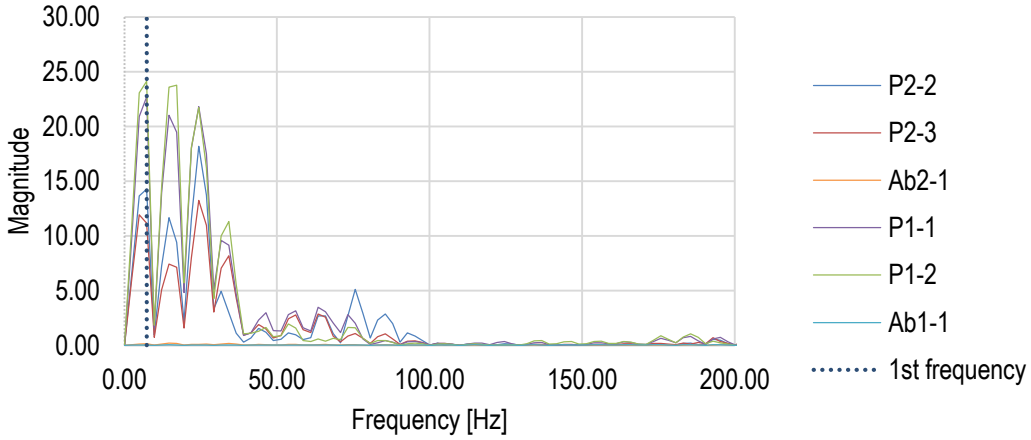

Figure 3.38: Frequency spectrum obtained from Y-accelerations of output points on the substructure. First natural frequency, equal to 7.33Hz is marked with dotted line.

Fast Fourier transform on the acceleration results gave the frequency spectrum of the structure. The first frequency was recovered quite well. The obtained ω_1 equals 7.33 Hz compared to 7.73 Hz from the free vibrations analysis. Figure 3.38 presents the frequency spectrum obtained from Y-accelerations of output points on the substructure. In Figure 3.39 the frequency spectrum obtained from Z-accelerations of output points on the superstructure is shown. First natural frequency, equal to 7.33 Hz is marked with dotted line on both figures.

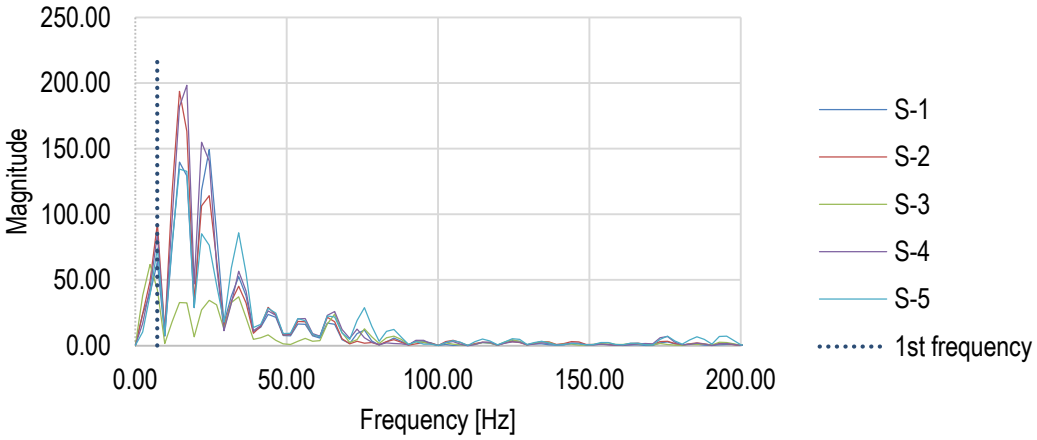

Figure 3.39: Frequency spectrum obtained from Z-accelerations of output points on the superstructure. First natural frequency, equal to 7.33 Hz is marked with dotted line.

3.5.2. The influence of maximum impact load P_{max}

Two values of P_{max} were chosen and the recorded accelerations were compared. As the responses showed the same trend, only the results for two points were shown where the amplitudes were the highest and the lowest. Figure 3.40 shows accelerations in Y-direction vs. time in the output point closest to the impact (point P2-2, point number 2 on Pier 2). Accelerations in Y-direction vs. time at the output point furthest from the impact (point Ab1-1, point number 1 on Abutment 1) are depicted in Figure 3.41. The curves retain the same character regardless of P_{max}. The acceleration amplitudes decrease when P_{max} goes down. For a two times lower maximum impact load, the amplitudes are approximately two times smaller.

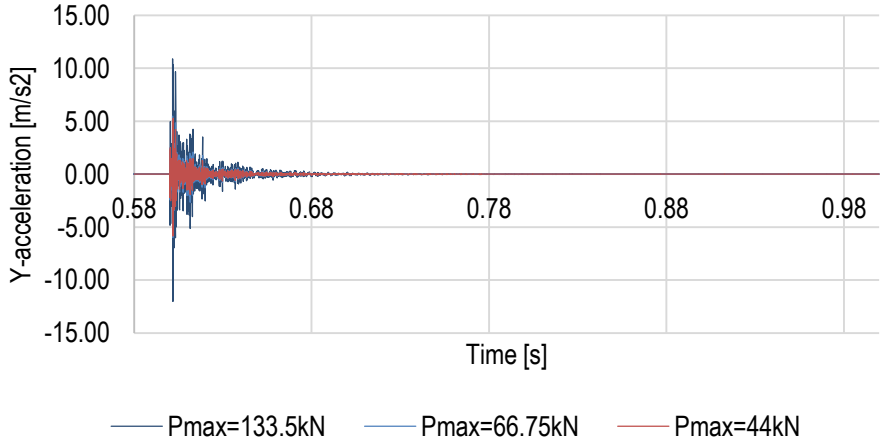

Figure 3.40: Accelerations in Y-direction vs. time in the output point closest to the impact (point P2-2, point number 2 on Pier 2)

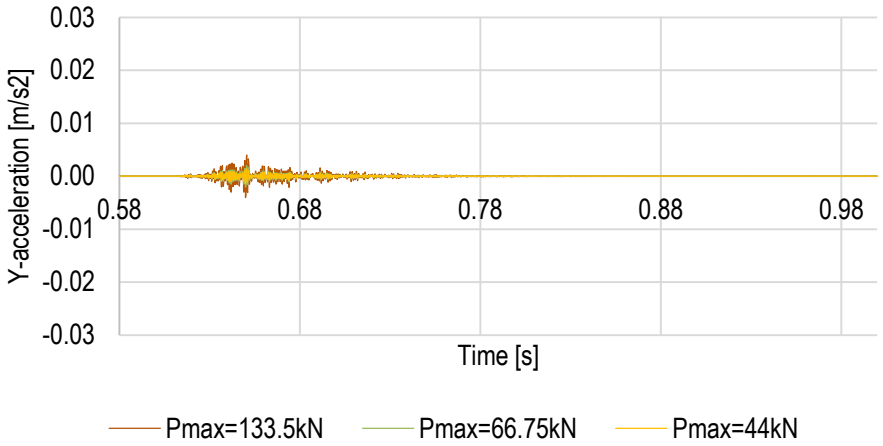

Figure 3.41: Accelerations in Y-direction vs. time in the output point furthest from the impact (point Ab1-1, point number 1 on Abutment 1)

3.5.3. Influence of cracks

The influence of the presence of cracks is studied in Test 3. Comparison of recorded accelerations for three models, without cracks, with 1 crack, and with 2 cracks, are presented in Figure 3.42. Small variations in extreme values of the accelerations as well as the curve shape are apparent. This gives a reason to suspect that measuring accelerations can be a good method for monitoring of the structure. Even though no assumptions can be made looking at a single acceleration vs. time curve, repeating the recordings over time may indicate that otherwise unnoticeable changes in the structure are occurring.

The frequency spectrum was established for every case. Frequency values obtained were exactly the same for both cases. This result was not surprising, as previous studies [11] showed that natural vibrations are insensitive to such small changes.

a)

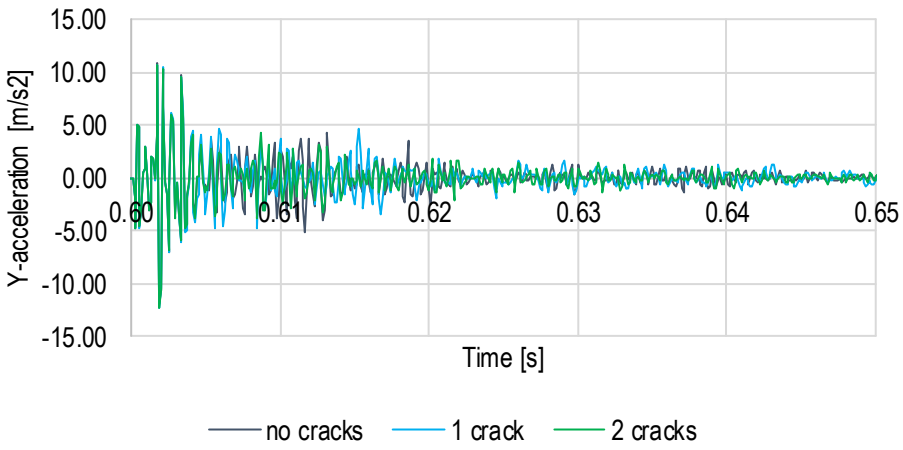

b)

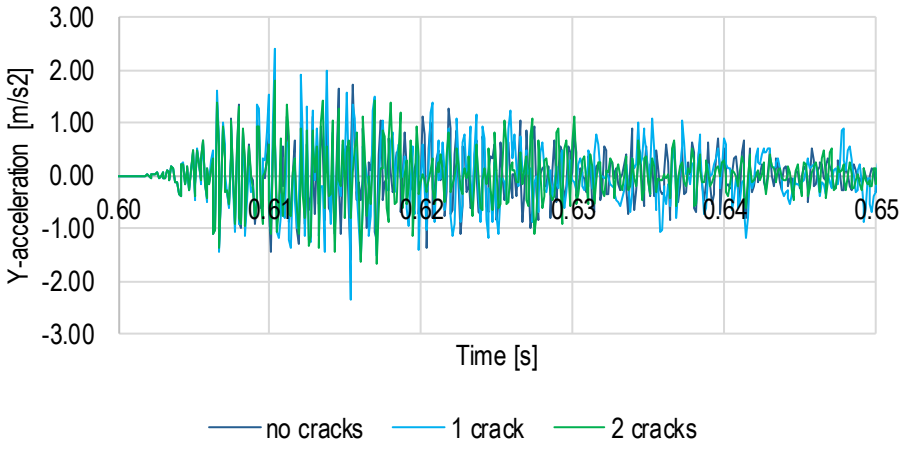
3.00
2.00
1.00
0.00
-1.00
-2.00
-3.00
Y-acceleration [m/s2]
0.60
0.61
0.62
0.63
0.64
0.65
Time [s]
no cracks
1 crack
2 cracks

c)

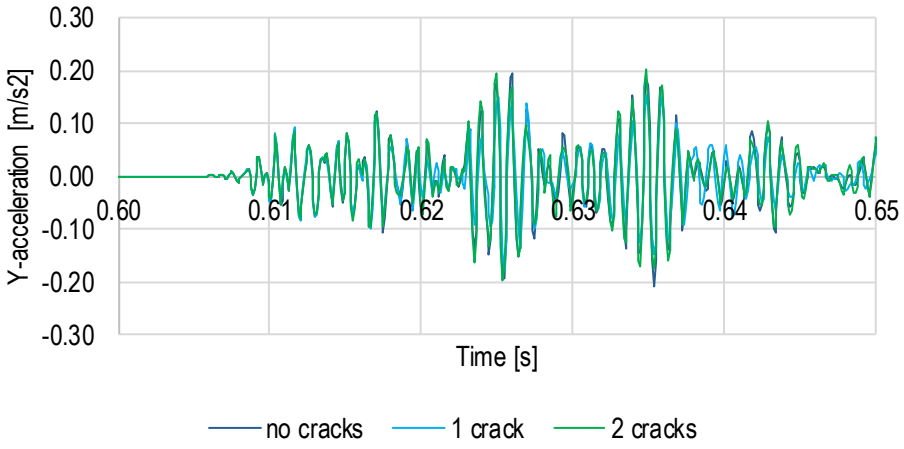
0.30
0.20
0.10
0.00
-0.10
-0.20
-0.30
Y-acceleration [m/s2]
0.60
0.61
0.62
0.63
0.64
0.65
Time [s]
no cracks
1 crack
2 cracks

d)

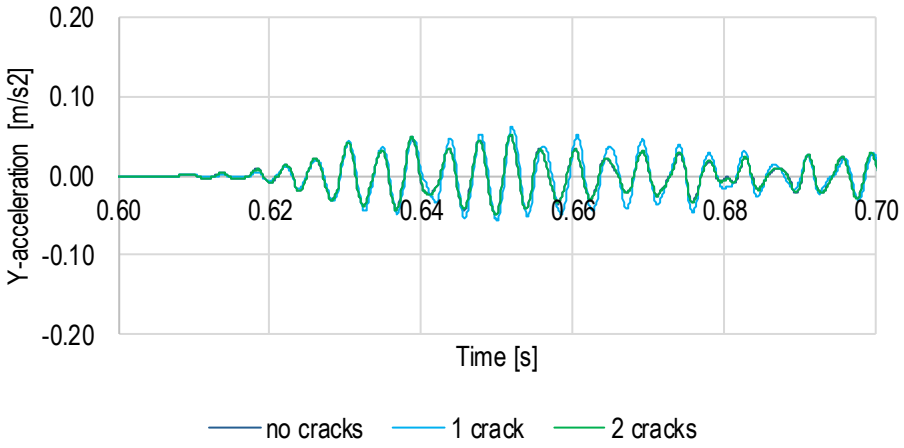
0.20
0.10
0.00
-0.10
-0.20
Y-acceleration [m/s2]
0.60
0.62
0.64
0.66
0.68
0.70
Time [s]
no cracks
1 crack
2 cracks

e)

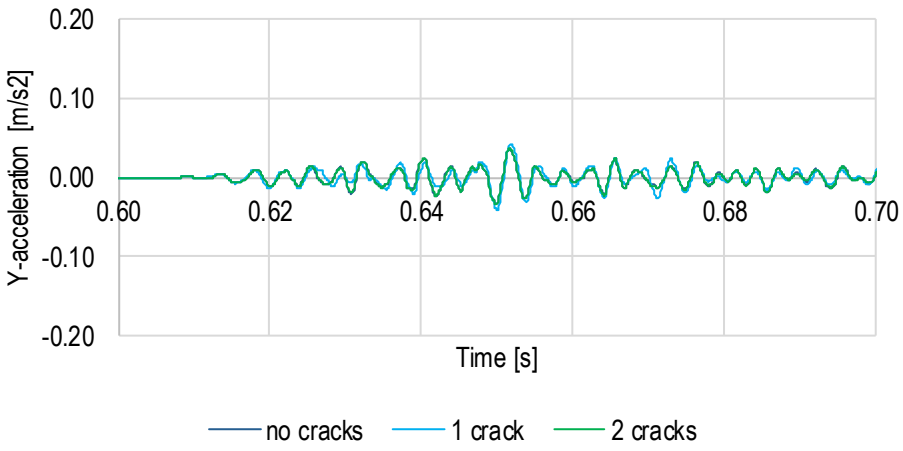

f)

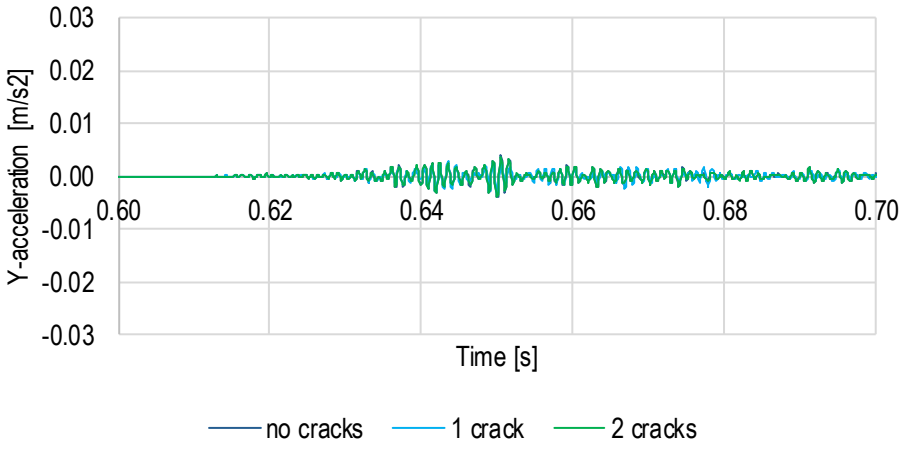

Figure 3.42: Acceleration in Y-direction at output nodes on the substructure a) P2-2, b) P2-3, c) Ab2-1, d) P1-1, e) P1-2, f) Ab1-1

3.5.4. Influence of impact locations

Impact load was applied at various points on the substructure. The locations were chosen on all supports, in the old and new sections. The purpose was to examine the way structural response changed due to the impact location. Figure 3.43 shows a graph of Y-acceleration vs. time recorded at output nodes on the substructure for impact point 2, which lays on the wall surface of Pier 2 on the SW side. Figure 3.44 presents Z-acceleration vs. time at output nodes on the superstructure for the same impact location. The next case considers impact at point 3, which is located on the top surface of Abutment 2 between first and second girder of the old part of the foundation. Figure 3.45 shows Y-acceleration vs. time at output nodes on the substructure and Figure 3.46 shows Z-acceleration vs. time at output nodes on the superstructure for impact at point 3. Point 4 is located on the wall of this abutment. The responses at the output points are presented in Figure 3.47 and Figure 3.48.

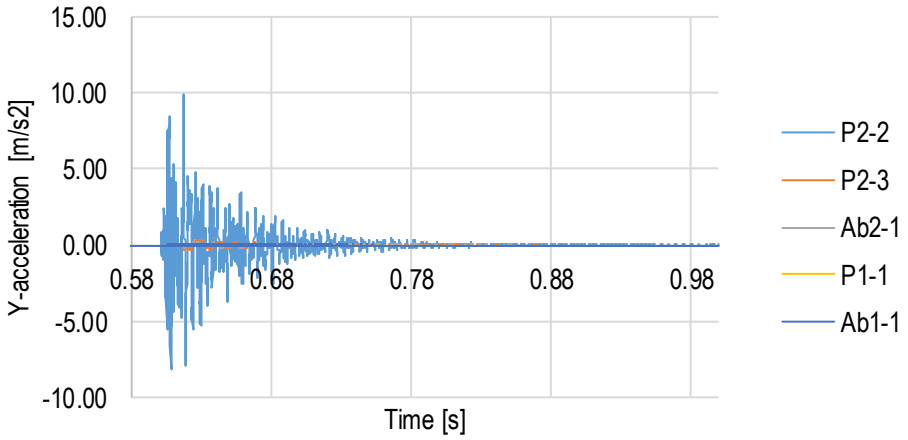

Figure 3.43: Y-acceleration vs. time at output nodes on the substructure for impact at point 2.

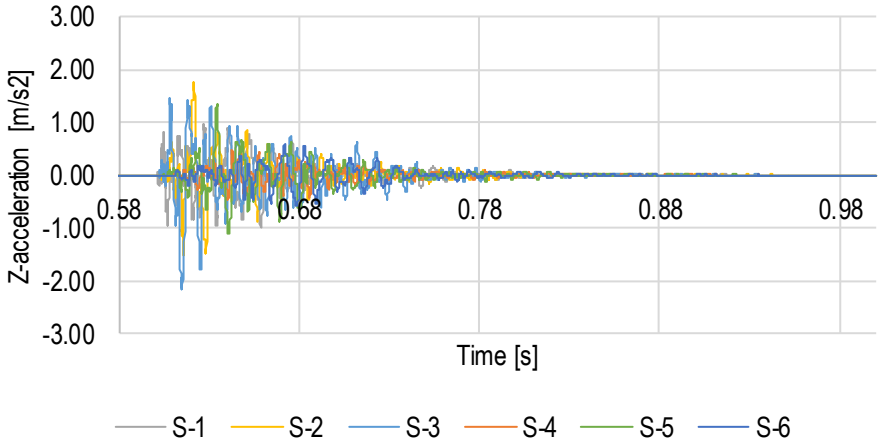

Figure 3.44: Z-acceleration vs. time at output nodes on the superstructure for impact at point 2.

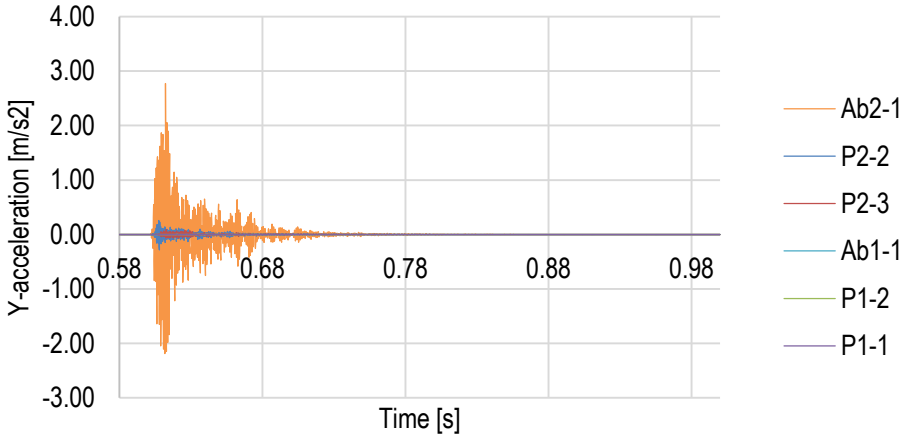

Figure 3.45: Y-acceleration vs. time at output nodes on the substructure for impact at point 3.

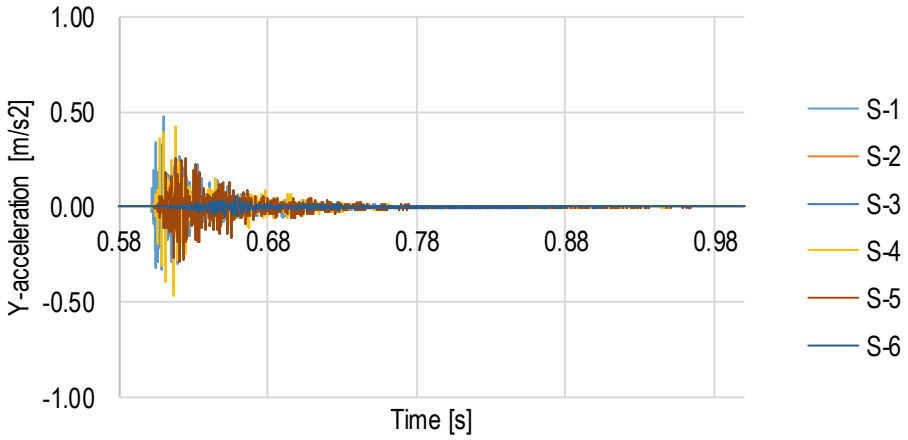

Figure 3.46: Z-acceleration vs. time at output nodes on the superstructure for impact at point 3.

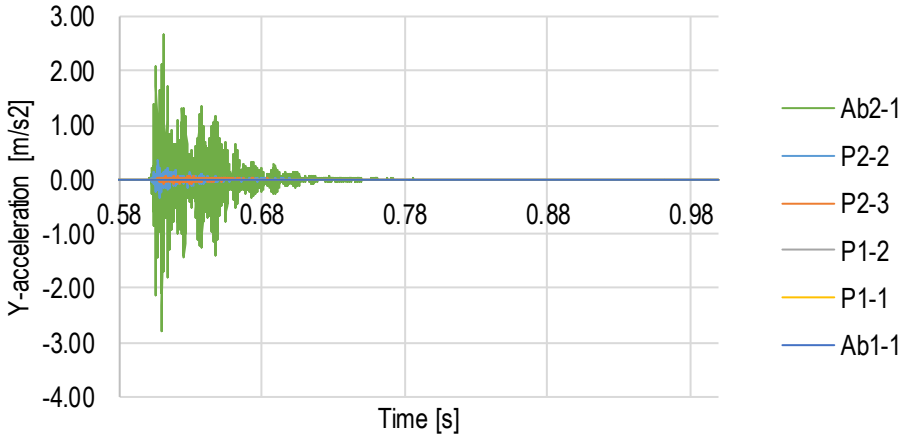

Figure 3.47: Y-acceleration vs. time at output nodes on the substructure for impact at point 4.

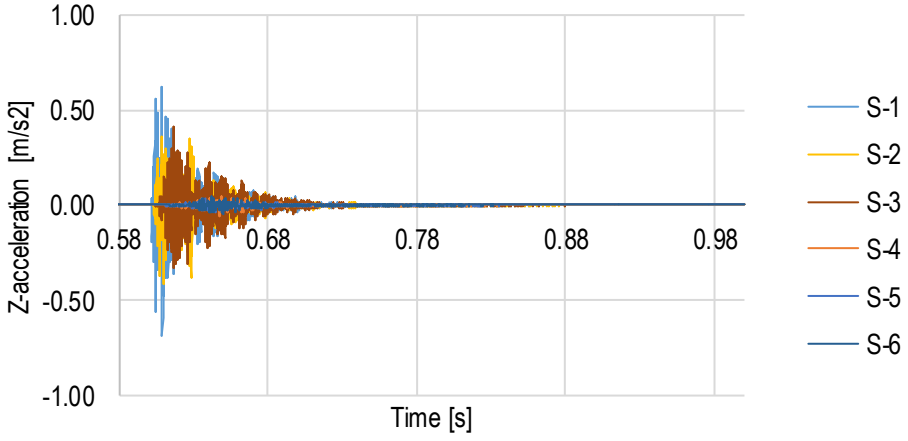

Figure 3.48: Z-acceleration vs. time at output nodes on the superstructure for impact at point 4.

Depending on the location of the impact load, the structural response differs. Accelerations are greater when the load is applied to the pier, and smaller when the abutment is subjected to the load. This difference might be caused by difference in the volume of the supports. The abutment is bigger than the pier and most of the wave is diffused in it. It is not distributed further into the other supports.

Vibrations are damped heavily by the structure. Although the model suggests that waves can be recorded on all supports, in real conditions the recordings at the furthest output points can be obscured by environmental noise. Proper sensors should be chosen and their effectiveness should be studied on site.

4. Conclusions

The presented computational model was developed based on the available data. The information obtained from the as-built drawings from 1934/1966 were used to get the shape and dimensions of the structure. They were also a source of general information on what structural materials were used during construction. The surveying measurements served as a confirmation of these data and also filled in the missing information.

Samples obtained from the boreholes drilled in all supports were tested in the laboratory. Only the basic tests were performed giving such properties as stiffness modulus, strength of the construction materials and bedrock, as well as friction angle and density of the overburden. These quantities were sufficient to use the 'simple input' material models for concrete, where the generation of model parameters is automatic and the elastic-plastic model was used for other materials. Due to the limitation in this regard, the model lacks a proper representation of nonhomogeneous masonry. In reality, the supports are made out of limestone masonry units connected with cement mortar. They are also cracked in some areas, e.g. the borings showed that Pier 2 and Abutment 2 are cracked vertically in the SW section. No details are known about the extent of these voids or the distribution of other cracks. To account for the lesser strength of the old section, the values of material parameters were decreased by 20% relative to the new section.

Despite the above mentioned issues, it was shown in this report that the developed numerical model can be used to simulate a range of different nondestructive tests and be used as a supplementations of the on-site tests. They are less time and cost consuming and yield values of state variables, like stress and strain, over the entire structure, not at a few test measurement points. The model predictions of structural behavior under various loads appear to be as accurate as the physical measurements. However, measured quantities were often near the limits of the equipment and further testing of the modeling for a bridge that is not on bedrock is recommended. Static, dynamic, and impulse loading cases were considered.

According to the model the differences in deck and substructure vertical displacements are significant. Maximum deck deflections go from about 5 mm in the base case (which includes only the gravity load of the structure) up to about 7 mm when the case of 130% of the deck weight is considered and up to about 10 mm in a dynamic load case. The supports show very small deformations, of the order of 0.01 mm or lower.

Maximum equivalent stress in the foundations were calculated and compared to the load-carrying capacity. According to the model, less than 5% of the structural capacity of the foundations is used. The margin of safety of the geotechnical capacity is also high (percentage of capacity used: less than 3.5%), therefore extending the analysis into the failure range was not needed for this case.

Structural monitoring for this particular structure could include monitoring of displacements, stresses, and accelerations. Even though, as previously stated, the deformations of foundations are relatively small, they can still be measured with appropriate sensors. It is recommended that they are placed in top sections of the foundations, where the displacements are the highest. The highest stress values, recorded on the bottom of the piers are impossible to

measure on-site. Nevertheless, mounting load cells in the boreholes will allow recording of stresses close to the extreme ones. Other locations of interest are below the bearings, on the foundation walls as the model shows stress concentrations there.

Another method that can be used for monitoring of the structure is impact testing. The simulations performed show that this technique allows detection of voids in the foundations. It must be stated that the model used homogeneous materials and therefore differences in response are clearly visible. The real structure is built of a nonhomogeneous materials and therefore the recordings will be different. Nonetheless, the method seems to be appropriate for structural monitoring, if the tests are repeated over time.

5. References

[1] Livermore Software Technology Corporation LS-PrePost Online documentation, http://lstc.com/lspp

[2] LS-DYNA Keyword User's Manual Vol.II, December 2014

[3] Lourenco P.J., Computational strategies for masonry structures, PhD Thesis, Netherlands, 1996

[4] Xanthakos P., Bridge substructure and foundation design, Prentice Hall, 1995

[5] Development of Geotechnical Resistance Factors and Downdrag Load Factors for LRFD. Reference Manual, publ. no. FHWA-NHI-05-052, February 2005

[6] AASHTO LRFD Bridge Design Specifications 5th Edition, 2010

[7] Wekezer J., Szurgott P., Kwasniewski L., Siervogel J., Investigation of Impact Factors for Permit Vehicles, 2008

[8] http://www.bksv.com/Products/transducers/vibration/impact-hammers/8210?tab=specifications

[9] Aktan A.E., Moon F.L., Structural Identification of Aged Reinforced Concrete Bridges, FHWA Project TPF-5(113)

[10] Irwin L.H., Orr D.P., Atkins D., Falling Weight Deflectometer Calibration Center and Operational Improvements Redevelopment of the Calibration Protocol and Equipment, FHWA-HRT-07-040, October 2011

[11] Aouad M.F., Olson L., Liu M.: Initial test results from FHWA Project "Dynamic Bridge Substructure Evaluation and Monitoring System", 1988, SPIE vol.3400, pp 44-54

Energy Systems Division
Argonne National Laboratory
9700 South Cass Avenue, Bldg. 362
Argonne, IL 60439-4815

www.anl.gov

Argonne National Laboratory is a U.S. Department of Energy laboratory managed by UChicago Argonne, LLC